



Enhanced PON Infrastructure Enabled by Silicon Photonics

Thèse

Mingyang Lyu

Doctorat en génie électrique
Philosophiæ doctor (Ph. D.)

Québec, Canada

Enhanced PON Infrastructure Enabled by Silicon Photonics

Thèse

Mingyang Lyu

Sous la direction de:

Leslie Ann Rusch, directrice de recherche

Résumé

Les systèmes de courte portée et de détection directe sont le dernier/premier kilomètre de la fourniture des services Internet d'aujourd'hui. Deux cas d'application sont abordés dans cette thèse, l'un concerne l'amélioration des performances des services Internet par la Fibre-To-The-Home ou les réseaux optiques passifs (PONs). L'autre est le radio access network (RAN) pour le fronthaul. Notre objectif pour RAN est de superposer les signaux 5G sur une infrastructure PON.

Nous démontrons expérimentalement la génération d'un signal de répartition multiplexée de fréquences orthogonales (OFDM) à bande latérale unique en utilisant un modulateur IQ sur puce basé sur les photoniques au silicium à micro-anneau. Il s'agit d'une solution à coût bas permettant aux PONs d'augmenter les débits de données grâce à l'utilisation d'OFDM. Nous avons généré un signal OFDM à large bande avec un ratio de suppression de bande latérale de plus de 18 dB. Afin de confirmer la robustesse de la dispersion chromatique (CD), nous transmettons le signal généré OFDM SSB dans plus de 20 km de fibre de monomode standard. Aucun fading induit par la CD n'a été observé et le taux d'erreur sur les bits était bon.

Nous proposons une solution de photoniques au silicium pour un réseau optique passif afin de mitiger l'interférence de battement signal-signal (SSBI) dans la transmission OFDM, et de récupérer une partie des porteuses de la liaison descendante pour une utilisation dans la liaison montante. Le sous-système recrée les interférences à une entrée du détecteur équilibré ; le signal de données corrompu par SSBI est à la deuxième entrée. L'annulation se produit via la soustraction dans la détection équilibrée. Comme notre solution de photoniques au silicium (SiP) ne peut pas filtrer les signaux idéalement, nous examinons un facteur d'échelle introduit dans la détection équilibrée qui peut balancer les effets de filtrage non idéaux. Nous montrons expérimentalement l'annulation de l'interférence donne de bonnes performances même avec une porteuse faible, soit pour un ratio porteuse/signal ultra bas de 0 dB. Bien que notre solution soit sensible aux effets de la température, notre démonstration expérimentale montre que le réglage de la fréquence résonante peut dériver jusqu'à 12 GHz de la valeur ciblée et présenter toujours de bonnes performances.

Nous effectuons des simulations extensives du schéma d'annulation SSBI proposé, et suggérons une diverse conception polarisée pour le sous-système SiP. Nous examinons via la simulation

la vulnérabilité à la variation de température et introduisons une nouvelle métrique de performance : Q-facteur minimum garanti. Nous nous servons de cette métrique pour évaluer la robustesse d'annulation SSBI contre la dérive de fréquence induite par les changements de température. Nous maximisons l'efficacité spectrale sous différentes conditions du système en balayant les paramètres de conception contrôlables. Finalement, les résultats de la simulation du système fournissent des indications sur la conception du résonateur micro-anneau, ainsi que sur le choix de la bande de garde et du format de modulation pour obtenir la plus grande efficacité spectrale.

Finalement, nous nous concentrons sur la superposition des signaux 5G sur une infrastructure PON pour RAN. Nous expérimentalement validons un sous-système photonique au silicium conçu pour les réseaux optiques passifs avec réutilisation de porteuses et compatibilité radio-sur-fibre (RoF) analogique 5G. Le sous-système permet la détection simultanée des signaux RoF et du signal PON transmis dans une seule tranche assignée de longueur d'onde. Tout en maintenant une qualité suffisante de détection des signaux RoF et PON, il n'y a que la puissance minimale de la porteuse qui est extraite pour chaque détection, ce qui conserve ainsi la puissance de la porteuse pour la modulation de liaison montante. Nous réalisons une suppression efficace du signal de liaison descendante en laissant une porteuse propre et forte pour la remodulation. Nous démontrons expérimentalement le signal RoF de liaison montante via un modulateur à micro-anneau. Nous avons détecté avec succès un signal à large bande de 8 GHz et cinq signaux RoF de 125 MHz simultanément. Et deux signaux RoF de 125 MHz sont remodulés sur la même porteuse. Le signal RoF de liaison montante généré est de 13 dB de plus que les signaux de liaison descendante, ce qui indique leur robustesse contre la diaphonie des signaux résiduels de la liaison descendante.

Abstract

Short reach, direct detection systems are the last/first mile of today's internet service provision. Two use cases are addressed in this thesis, one is for enhancing performance of Internet services on fiber-to-the-home or passive optical networks (PON). The other is radio access networks (RAN) for fronthaul. Our focus for RAN is to overlay 5G signals on a PON infrastructure.

We experimentally demonstrate the generation of a single-sideband orthogonal frequency division multiplexed (OFDM) signal using an on-chip silicon photonics microring-based IQ modulator. This is a low cost solution enabling PONs to increase data rates through the use of OFDM. We generated a wideband OFDM signal with over 18 dB sideband suppression ratio. To confirm chromatic dispersion (CD) robustness, we transmit the generated SSB OFDM signal over 20 km of standard single mode fiber. No CD-induced fading was observed and bit error rate was good.

We propose a silicon photonics solution for a passive optical network to mitigate signal-signal beat interference (SSBI) in OFDM transmission, and to recuperate a part of the downlink carrier for use in the uplink. The subsystem recreates the interference at one balanced detector input; the data signal corrupted with SSBI is at the second input. Cancellation occurs via subtraction in the balanced detection. As our silicon photonics (SiP) solution cannot filter the signals ideally, we examine a scaling factor to be introduced to the balanced detection that can trade-off the non-ideal filtering effects. We show experimentally that the interference is cancelled, allowing good performance even with a weak carrier, that is, for ultra low carrier to signal ratio of 0 dB. Although our solution is sensitive to temperature effects, our experimental demonstration shows the tuning of the resonant frequency can drift by as much as 12 GHz from the targeted value and still provide good performance.

We perform extensive simulations of the proposed SSBI cancellation scheme, and suggest a polarization diverse design for the SiP subsystem. We examine via simulation the vulnerability to temperature variation and introduce a new performance metric: minimum guaranteed Q-factor. We use this metric to evaluate the SSBI cancellation robustness against the frequency drift induced by temperature changes. We maximize the spectral efficiency under different system conditions by sweeping the controllable design parameters. Finally the system simulation results provide guidance on the microring resonator design, as well as choice of guard

band and modulation format to achieve the highest spectral efficiency.

Finally, we turn to focus on overlay 5G signals on a PON infrastructure for RAN. We experimentally validate a silicon photonic subsystem designed for passive optical networks with carrier reuse and 5G analog radio-over-fiber (RoF) compatibility. The subsystem enables the simultaneous detection of RoF signals and a PON signal transmitted in a single assigned wavelength slot. While maintaining sufficient quality of RoF and PON signal detection, only the minimum carrier power is leached off for each detection, thus conserving carrier power for uplink modulation. We realize effective downlink signal suppression to leave a clean and strong carrier for remodulation. We demonstrate experimentally the RoF uplink signal via a micro ring modulator. We successfully detected an 8 GHz broadband signal and five 125 MHz RoF signals simultaneously. And two 125 MHz radio over fiber signals are remodulated onto the same carrier. The generated uplink RoF signal is 13 dB over the downlink signals, indicating their robustness against the crosstalk from residual downlink signals.

Contents

Résumé	iii
Abstract	v
Contents	vii
List of Tables	ix
List of Figures	x
List of Abbreviation and Symbol	xii
Acknowledgements	xvii
Foreword	xviii
Introduction	1
I.1 Motivation	1
I.2 Project Outline	3
I.3 Thesis Outline	6
1 Silicon Microring IQ Modulator Enabled Single-Sideband OFDM transmission	9
1.1 Résumé	9
1.2 Abstract	9
1.3 Context and Contributions	10
1.4 Introduction	10
1.5 Device Design and Characterization	11
1.6 Experimental Setup	12
1.7 Experimental Results	13
1.8 Conclusion	17
2 SiP-based SSBI Cancellation for OFDM	18
2.1 Résumé	18
2.2 Abstract	19
2.3 Context and Contributions	19
2.4 Introduction	20
2.5 System Design	21
2.6 The Effect of Non-ideal Filtering Effect	23

2.7	Experimental Results and discussion	27
2.8	Discussion	32
2.9	Conclusion	34
3	Optimizing SiP Microring Resonators to Suppress Interference in OFDM Detection	36
3.1	Résumé	36
3.2	Abstract	36
3.3	Context and Contributions	37
3.4	Introduction	37
3.5	SSBI cancellation using MRR	38
3.6	Simulation Results	42
3.7	Conclusion	45
4	Silicon Photonic Subsystem for Broadband and RoF Detection While Enabling Carrier Reuse	46
4.1	Résumé	46
4.2	Abstract	46
4.3	Context and Contributions	47
4.4	Introduction	47
4.5	Subsystem Design	48
4.6	Experimental Setup	50
4.7	Hybrid Broadband and RoF detection	52
4.8	Carrier Reuse	55
4.9	Conclusion	59
	Conclusion and Outlook	61
II.1	Conclusion	61
II.2	Improved Designs for Future Work	63
	Publication	66
	Bibliography	68

List of Tables

2.1	Comparison of CSR and ADC requirements for different DD-SSB schemes with 30 dB received OSNR and 200 Gbits/s net data rate	33
3.1	MRR design guide at 25 db OSNR for optimizing SSBI cancellation; best kappa and offset are the κ and MRR frequency offset setting yielding highest spectral efficiency	45

List of Figures

I.1	PON revenue forecast from Omdia [2]	2
I.2	Global market for optical transceivers, AOCs and EOMs by technology [5] . . .	3
1.1	Schematic and microscope image of an optical SSB transmitter based on silicon microring IQ modulator.	11
1.2	(a) Partial mask layout for MRM1/MRM2, (b) cross section of the p-n junction of MRM1/MRM2 showing relevant dimensions, for MRM1 measured (c) power transmission spectra at different bias voltages, and (d) electro-optic frequency response (S21) at different frequency detunings.	12
1.3	Experimental setup	13
1.4	Optical spectrum of SSB-OFDM signal before transmission in dark grey and after 20 km transmission in light grey.	14
1.5	Received electrical spectrum and constellations for after transmission over 20 km of SSMF of (a) SSB-OFDM signal of Fig. 1.4, and (b) a DSB-OFDM signal; insets show constellation of subcarrier number 191.	15
1.6	Estimated SNR per subcarrier for SSB signal (solid blue curve) and DSB signal (dashed red curve)	16
1.7	BER of detected SSB-OFDM signal with varied received power.	16
2.1	Optical SSBI cancellation scheme with ideal carrier suppression	22
2.2	Non-ideal filtering effect	23
2.3	a) Carrier and OFDM placement vis-à-vis offsets. Electrical spectrum components for different cases of frequency offset, b) notch at carrier, c) notch more distant from OFDM signal, and d) notch closer to OFDM signal	23
2.4	Simulation system setup	24
2.5	Simulation of SSBI cancellation performance via different frequency offsets ($\alpha = 1$)	25
2.6	Simulation of Q-factor per subcarrier with varying α for $\kappa = 0.45$ and 10 GHz frequency offset	26
2.7	Simulation of SSBI cancellation performance via different frequency offsets (α optimized)	26
2.8	Characterization of new MRR	28
2.9	Experimental Setup; as identical photodetectors were not available, a single photodetector is time multiplexed	29
2.10	Electrical spectrum of a) signal plus SSBI noise (blue/dark) and isolated SSBI (yellow/light colored), and b) signal plus SSBI noise (blue/dark) and signal with suppressed SSBI (green/light colored)	30
2.11	Q-factor per subcarrier	31

2.12	Q-factor improvement[36] in dB due to SSBI cancellation vs. frequency offset for the three values of CSR. Proof-of-concept demonstration [32] results in square markers are included for comparison.	32
3.1	SSBI cancellation subsystem a) as examined experimentally in [48], and b) altered to achieve polarization diversity and tunable scaling factor.	38
3.2	MRR frequency response in the through port for various κ parameters	39
3.3	Q-factor vs. frequency offset for various κ ; illustrations of two sets of 8 and 16 GHz spans and the guaranteed minimum Q within that span (one set for $\kappa = 0.2$ and one set for $\kappa = 0.5$).	40
3.4	Color gives peak Q in dB (zero drift) at 0 dB CSR as a function of guard band and kappa; achievable QAM modulation for 10^{-3} BER indicated on appropriate contour and annotated with required Q.	42
3.5	Color gives peak Q in dB (zero drift) as a function of guard band and kappa; CSR is varied per graph, and color scale as in Fig. 3.4.	43
3.6	Color gives minimum guaranteed Q in dB for a drift spanning 12 GHz; color scale as in Fig. 3.4; CSR varied per graph, and color scale as in Fig. 3.4.	44
3.7	Spectral efficiency in bits/s/Hz at 25 dB OSNR, 5 dB CSR for four spans of frequency drift (4, 8, 12 and 16 GHz); 32QAM modulation unless otherwise labeled.	44
4.1	Principle of operation of the SiP subsystem. MRR drop ports are not shown.	49
4.2	Experimental setup to test subsystem.	51
4.3	(a) Mask layout of MRR set1; (b) MRR responses with thermal tuning	52
4.4	Optical spectrum at three measurement points: black curve is input to chip, red curve is output of MRR set 1, blue curve is output of MRR set 2; frequency responses of each set of cascaded MRRs are sketched in dotted lines; an inset zooms on the carrier to show carrier power dropped by MRRs.	53
4.5	Electrical spectrum of detection of (a) RoF signal, (b) OFDM signal.	54
4.6	MRM (a) partial mask layout, (b) cross section showing relevant dimensions, and (c) measured power transmission spectra at different bias voltages.	55
4.7	Uplink RoF signals with downlink RoF signals	56
4.8	Remodulated uplink signal (a) optical spectrum and (b) electrical spectrum	57
4.9	Automatic Ring Control	59
II.1	Layout of full design	63
II.2	Layout of transceiver with polarization diversity	64
II.3	Layout of 5G transceiver with polarization diversity	65
II.4	Layout of polarization division multiplexing with KK scheme	65
II.5	Layout of polarization solution with reduced devices	65

List of Abbreviation and Symbol

α	scaling factor
η	spectral efficiency
κ	coupling coefficient
$f(h)$	frequency response
AAU	active antenna unit
ADC	analog-to-digital converter
AOC	active optical cable
ASE	amplified spontaneous emission
AWGN	additive white Gaussian noise
BBU	base band unit
BER	bit error rate
BPSK	binary-phase-shift-keying
CD	chromatic dispersion
CMOS	complementary metal oxide semiconductor
CPRI	common public radio interface
CSP	communication service provider
CSR	carrier signal ratio
DAC	digital-to-analog converter

DC direction coupler

DD direct detection

DSP digital signal processing

EDFA erbium-doped fiber amplifier

EOM electro-optical modulator

ER extinction ration

EVM error vector magnitude

FDTD full-wave finite difference time domain

FEC forward error correction

FFT fast Fourier transform

FSR free spectral range

FWHM full width half maximum

IL insertion loss

ISP Internet service provider

LO local oscillator

MMI multimode interference coupler

MRM microring modulator

MRR microring resonator

MZI Mach-Zehnder interferometer

MZM Mach-Zehnder modulator

OFDM orthogonal frequency division multiplexing

ONU optical network unit

OSA optical spectrum analyzer

OSNR optical signal-to-noise ratio

PC polarization controller

PCB printed circuit board

PD photodetector

PDL polarization dependent loss

PIC photonic integrated circuit

PON passive optical network

PRBS pseudo random bit sequence

PSR polarization splitter rotator

QAM quadrature amplitude modulation

QPSK quadrature phase shift keying

RRU remote radio unit

RTO real-time oscilloscope

SiP silicon photonics

SNR signal-to-noise ratio

SOI silicon-on-insulator

SPS sample per symbol

SSBI signal to signal beating interference

TIA trans-impedance amplifier

VOA variable optical attenuator

WDM wavelength division multiplexed

*I never know what happens to my
experiments. Unexpected results
are expected in every experiment.
Optimization is always producing
worse results.*

*But I know there must be a
physical explanation for every
tricky phenomenon. Work on it
and I will reach that point. I hate
it but I'm addicted to it.*

We know the past but cannot
control it. We control the future
but cannot know it.

Claude Shannon

Acknowledgements

Firstly I would like to thank my parents for supporting me to finish this degree so I can really focus on my researches. I love them and I know they love me too.

Then I would like to thank my supervisor, Professor Leslie for guiding me to finish all the works. And I must thank professor Wei Shi for his advice and guides on my research these years.

I would like to thank the jury members for spending time on my thesis, which represents an unforgettable journey in these years. I am so happy to share my work with you. It will never be perfect, but I am proud of it.

Of course I have to write a long list of my friends to show how I am grateful for having them. I started the journey with Sasan and Alessandro. We support each other for all these years. For Yuxuan, Jiachuan, Yelong, Zhongjin and all your families, thanks for your support and help these years. And for Wen, Simin, Haoxin and Weichen, I am so thankful that you could support me through the toughest period.

I never thought what kind of person I wanted to be. I did not love myself in the past. I made some irrational decisions and was so hurried to finish things like there were tasks and deadlines for my life. I would like to thank Leslie for all the things she told me. She shared my bad feelings patiently and guided me kindly. That was the darkest time I experienced. But we make it. I love myself, as a person. I am a mess but I could do good things. That is human.

At the end, I want to show my love to my beloved Corgi Oriana.

Foreword

Four chapters of this thesis are based on the materials published in conferences and journal papers. I am the main contributor for all the publications mentioned. Detailed contribution of co-authors is provided in following.

Most of the contents in following four chapters are the same as the journal papers while the chapters include minor modifications to provide better coherence to the thesis. Supplemental details are also provided.

Chapter 2: Lyu, Mingyang, Yelong Xu, Leslie Rusch and Wei Shi. "Single-Sideband OFDM Transmission via a Silicon Microring IQ Modulator." *IEEE Photonics Technology Letters* 31.2 (2018): 145-148. This paper is submitted at December, 2018 and accepted in December, 2018.

In this paper, we demonstrate for the first time the single sideband OFDM transmission via micro ring based IQ modulator.

This chip was designed by Prof. Shi and fabricated via IMEC process. Postdoc Yelong Xu characterized the chips and was responsible for coupling light onto the chip and probing the RF signals. I was responsible for the application scenario (single sideband OFDM), including generating all data, capturing received signals, and processing digital signals offline. Postdoc Yelong Xu wrote the ring modulator related part of the paper and I wrote the rest. This paper was revised by Prof. Shi and Prof. Rusch.

Chapter 3: Lyu, Mingyang, Wei Shi, and Leslie Rusch. "SiP-based SSBI Cancellation for OFDM." *IEEE Photonics Journal* This paper is submitted at August, 2018 and published at May, 2019.

This paper demonstrates for the first time a silicon photonics solution under passive optical network scenario both to reduce signal-to-signal beat interference and to recuperate part of the downlink carrier for the uplink. The robustness to frequency drift, as well as the impact of impact of imperfect filtering, is discussed and quantified.

I designed the subsystem in the chip used in this paper under the guidance of Prof. Shi, particularly the microring resonator design. The photodetector on chip was designed by PhD student Jonathan St Yves, while other components are standard designs from SiEPIC library.

I completed the layout and submitted the design for fabrication via the IME process. I characterized the fabricated chip in the COPL laboratory.

Prof. Rusch provided guidance for the system experiments, with support from Prof. Shi on the thermal robustness. I completed simulations to guide the experiment. I built the setup and ran the data transmission experiments with offline data processing. The paper was written by me and revised by Prof. Shi and Prof. Rusch.

Chapter 4: Lyu, Mingyang, Wei Shi, and Leslie Rusch. "Optimizing SiP Microring Resonators to Suppress Interference in OFDM Detection" Submitted to IEEE Optical Express (May, 2021).

In this paper, we run the systematic analysis on the previously proposed SSBI cancellation scheme. We introduce a new performance metric, minimum guaranteed Q, to evaluate the system under fluctuating operation point. The systematic simulation provides guidance on the microring resonator design as well as the guard band value and modulation format choice to achieve the highest spectral efficiency.

I designed the original subsystem as mentioned in Chapter 1 and the following enhancement on polarization diversity. The idea of minimum guaranteed Q is proposed via the discussions with Prof. Rusch. I completed simulations. Prof. Rusch provided guidance for process on the simulation results. The paper was written by me and revised by Prof. Rusch.

Chapter 5: Lyu, Mingyang, Wei Shi, and Leslie Rusch. "Silicon Photonic Subsystem for Broadband and RoF Detection While Enabling Carrier Reuse" Optics Express 28.10(2020). This paper is submitted at Feb, 2020 and accepted at may, 2020.

In this paper, we propose and experimentally validate a silicon photonics ONU subsystem for next generation passive optical networks with carrier reuse, enabling radio over fiber to share assigned wavelength slots.

I designed subsystem in the chip used in this paper under the guidance of Prof. Shi and Prof. Rusch. The idea of ONU subsystem compatible to radio over fiber signal comes from Prof. Rusch and Prof. Shi. I simulated and designed the cascaded ring resonators. The micro ring modulator was designed by Yelong Xu while other components are standard designs from SiEPIC library. The chip used in this paper was fabricated via IME process. I characterized the fabricated chip in the COPL laboratory.

Prof. Rusch provided guidance for the system experiments. I built the setup and ran the data transmission experiments with offline data processing. The paper was written by me and revised by Prof. Shi and Prof. Rusch.

Introduction

I.1 Motivation

We live in an age of data. Every aspect of life is closely related to the data stream, which is mostly carried through the optical communication infrastructure. Pushed by the new applications such as artificial intelligence, internet of things and edge computing, the demand for higher speed communication services will never stop. Two-thirds of the world's current data was newly generated through the past five years. According to research at IDC [1], the datasphere will be more than 5X larger in the next five years.

As discussed in the report from Omdia [2], fixed broadband links are providing connections for more than 1.1 billion households. The number of connections is increasing by 16 million every quarter year. In particular, the importance of communication infrastructure was proved beyond imagination through the 2020 pandemic. Enabled by the broadband-to-the-home ecosystem, billions of people could work from home, study from home and even connect with other people through video conferences.

Within this ecosystem, passive optical networks (PONs) play an extremely important role. PONs have a point-to-multipoint architecture. By centralizing the processing in one optical line terminal at the central office and communicating with simple user side units, optical network units (ONUs), power consumption and network management can be improved significantly. Due to urgent bandwidth capacity demand increases, the landscape of PON has expanded dramatically. Over 600 millions premises are supported by PON [2]. The ability of supporting new revenue streams over the same optical distributed networks attracts more vendors and Internet service providers (ISPs) into the market. With the upgrade of 10G PON ramps up in many countries, next generation of PON is under discussion.

A single fiber feeder structure keeps PON costs down. Internet service providers can PON infrastructure reuse for different scenarios, including enterprise services, xHaul as well as the network slicing. This trend pushes the ability to support new features for next generation PONs.

The network slicing enabled by software defined access would allow the next generation PON to

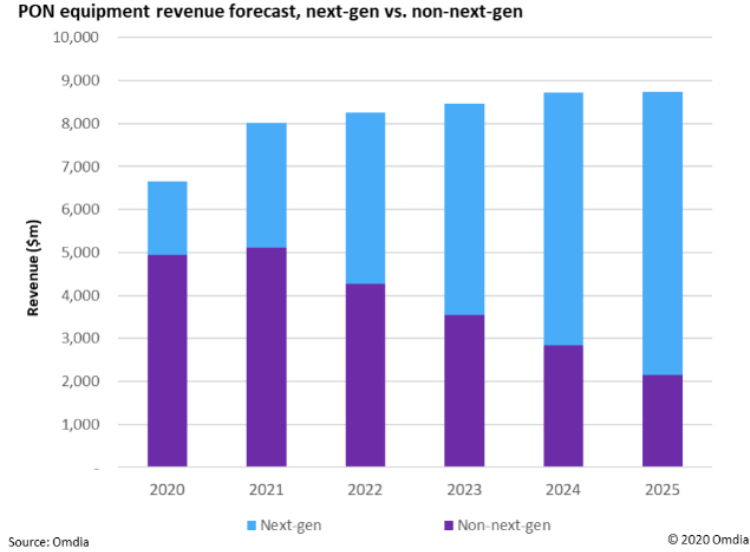


Figure I.1: PON revenue forecast from Omdia [2]

support different virtual networks for different applications. To meet the new requirements, the optical network units should remain colorless for easy management. Future PONs should also be able to support multiplexing in the time domain as well as in wavelengths [3]. Orthogonal frequency division multiplexing (OFDM) is promising for PON systems, as it is a particularly flexible solution for sculpting both the time and frequency domains.

Given the wide PON deployment, they are also a ready infrastructure that could be exploited to carry radio access signals as well as traditional Internet services. By radio access we refer to xHaul that includes the fronthaul, midhaul and backhaul of access network [4]. Mobile backhaul for 4G data-streams are already carried on some PONs. The densification of 5G will require a huge number of small cells. The topology of PON exhibits significant cost advantage and makes PON an attractive solution for carrying more than backhaul of 5G.

To exploit PONs for radio access, components must be very cost effective. All of our solutions are based on the technique of silicon photonics in order to meet this requirement. Driven by the growing demand of higher performance and higher density at equal or even lower cost, adoption of silicon photonics is reaching an inflection point. Current InP and GaAs optics are limited by the reliability and incompatibility to complementary metal oxide semiconductor (CMOS) electronics. In contrast, benefiting from the mature CMOS fabrication process, silicon photonics provides low cost and compact solutions. The trend of co-packaging between optics and CMOS based switching application-specific integrated circuits and field-programmable gate arrays also pushes the industry towards silicon photonics. The Fig. I.2 shows the prediction of global market for optical transceivers, active optical cables (AOCs) and electro-optical modulators (EOMs). The market share of solutions with silicon photonics

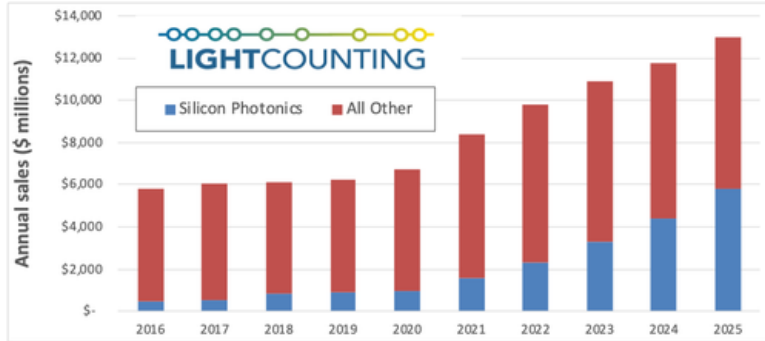


Figure I.2: Global market for optical transceivers, AOCs and EOMs by technology [5]

is increased from 14% at 2018 to 45% by 2025. These trends motivate our focus on silicon photonics (SiP), anticipating its wide adoption.

Promised improvements of 5G (such as low latency and high throughput) can be enabled and enhanced via the exploitation of optical networks. Thus the common vision for 5G is that it should leverage both optical and wireless innovative technologies. Thanks to fiber to the home (FTTH), optical fibres are more available now. PONs provide a ready solution for supporting the sheer number of small cells required for 5G. In synergy with PONs, analog RoF technologies can further alleviate the deployment cost by simplifying the ONUs. At the same time, massive silicon photonics based products appearing at the market could dramatically reduce the cost of optical components like transceivers and passive optics.

I.2 Project Outline

Short reach, direct detection systems are the last/first mile of today’s internet service provision. Two use cases are addressed in this thesis, one is for enhancing performance of Internet services on FTTH or PON. The other is radio access networks (RAN) for fronthaul. Our focus for RAN is to overlay 5G signals on a PON infrastructure.

I.2.1 Enhancing performance of PON digital services

PONs are cost sensitive and solutions should respect this constraint. Hence we focus on the use of SiP to achieve performance enhancement. We assume direct detection (DD) for the same reason. We examine optical OFDM in our work for its simple receiver structure. The wide adoption of OFDM in the telecommunications industry assures extensive know-how for cost effective OFDM receivers.

The transmission distance of DD-OFDM is limited by chromatic dispersion (CD). Two sidebands of double sideband (DSB) OFDM suffers opposite dispersion effect, resulting in destructive interference after beating with the carrier. Frequency-related power fading severely

limits the performance, especially for wider bandwidth signals and longer distance transmission. In contrast, single sideband (SSB) OFDM avoids dispersion induced power fading and could potentially double the spectral efficiency. The generation of SSB-OFDM could be realized by implementing a sideband rejection filter. However, the requirement of sharp filters with fine frequency control makes the filtering method less attractive. We choose the complex modulation method to generate the SSB-OFDM; we examine a two ring, microring modulator implementation. This solution has a significantly smaller footprint compared to other SiP solutions, with the added advantage of lower power consumption compared to using Mach-Zehnder modulator (MZM) based IQ modulator.

Once the dispersion induced performance degradation is avoided, the key limiting factor for longer transmission distance becomes signal beating interference (SSBI). After photodetector, beating between signal and carrier generates the original signal. At the same time, beating between signal itself will mix with the desired part, which is called SSBI.

There are four approaches to deal with SSBI. In the first method, the carrier boosting [6] approach, the carrier is amplified with an erbium-doped fiber amplifier (EDFA) to achieve higher carrier to signal ratio (CSR). When CSR is high, SSBI will be negligible compared with the detected signal. In the second method, SSBI is avoided by inserting a guard band as large as the data spectrum [7]. SSBI will fall out of band, but the spectral efficiency is halved in this method. In the third method, signal processing approach, SSBI is interactively reconstructed and subtracted using digital signal processing (DSP) [8].

Those methods are not suitable in PONs. In PONs the carrier is also reused for uplink modulation to achieve colorless operation. This limits the power budget, thus carrier power may not be sufficient to achieve the high CSR required to suppress the SSBI effect using the first method. The sacrifice of the spectral efficiency in the second method ultimately limits data rate. The third method requires high speed electronics and increases the power consumption.

The fourth method is hardware SSBI cancellation and is most appropriate for PONs. Optical signal processing creates a copy of SSBI and subtracts it to leave the OFDM signal free of SSBI. This has been examined analytically [9] and experimentally using discrete components [10]. However, the hardware approach is limited by the high system complexity using discrete components. We experimentally examined the use of silicon photonics to overcome this limitation. We design the micro ring resonator to achieve the carrier suppression function required for SSBI cancellation.

While polarization and temperature sensitivity pose challenges when using SiP, we proposed an enhanced SSBI cancellation scheme with polarization diversity. We complete extensive simulations to elucidate the design compromises. We explore the impact of temperature variation and the strategy for detuning of the center frequency of SSBI cancellation filter. We

demonstrate via simulation that SiP SSBI cancellation could be very effective and temperature robust, which is suitable for cost sensitive PONs.

I.2.2 Radio Access Networks over PON

Our second focus is on exploiting the PON infrastructure to support RAN for 5G signals. The 5G signals would be overlaid on the PON signals for Internet service. At present, RAN signals are produced by digitizing the RF signals to respect the common public radio interface (CPRI) interface [11]. The inefficiency of CPRI becomes more and more problematic for 5G. For the main stream configuration of 5G, 64 antennas supporting 100 MHz bandwidth lead to a total data rate of 172.8 Gbps at CPRI interface. The consequent sharp increase cost of implementing high speed optical module is unacceptable for the communication carriers.

To meet the 5G requirement, eCPRI is developed. The fundamental reason for the low efficiency of CPRI is that more information will be added to the original data stream through different communication protocol layers, resulting in bulky frames at the end of physical layer. To improve the efficiency, eCPRI moves the processing in low physical layer (PHY) to the remote radio unit (RRU), which is called AAU (active antenna unit) then. The data stream between base band unit (BBU) and AAU is significantly reduced at the cost of increasing AAU complexity. For current standard specifications, eCPRI will be sufficient for most cases. However, eCPRI will hit a new bottlenecks as 5G moves to greater numbers of antennas.

Compared to the digitized radio signal over fiber techniques, analog radio signals are promising candidates to handle future radio signals, if only due to the sheer number of small cells. We examine the radio over fiber (RoF) technique that directly modulates the analog radio signals onto the carrier in the central office and transmits the signal in fiber. The remote antenna units perform a simple optical-electrical (OE) conversion and then emit the analog radio signal. Compared to CPRI, spectral efficiency could be dramatically increased and the cost lowered. The analog signal is more vulnerable than a digital signal to impairments, yielding shorter transmission distance. Due to the dense nature of 5G cells, the transmission distance limit will be less problematic.

We propose an integrated transceiver solution for PON with carrier reuse. We experimentally demonstrate an ONU subsystem to support overlaying the 5G RoF signal on the traditional PON traffic. Cascaded microring resonators provide compact solution for isolating the hybrid signals. To further decrease the power consumption, we re-modulate the carrier to generate the uplink signal via an on-chip microring modulator (MRM). The ONU subsystem is experimentally demonstrated as an integrated and low cost solution for the overlay of 5G signal over PON infrastructure.

I.3 Thesis Outline

This thesis discusses two cases: one is digital data on FTTH or PON and the other is overlay 5G signals on a PON infrastructure for RAN. All cases are based on the silicon photonics technology, yielding compact and cost-effective solutions.

This thesis is comprised of four chapters following this introduction. Chapters 1 to 3 discuss the digital data on FTTH or PON. In chapter 1 we experimentally demonstrate the generation of SSB OFDM signal via silicon IQ configured MRMs. After 20 km of standard single-mode fiber transmission without CD compensation, the bit error rate is verified to be well under forward error correction (FEC) threshold. In chapter 2 we propose a SiP based solution to mitigate SSBI in direct detection. Uniformed performance of all subcarriers under ultra low CSR (0 dB) was experimentally verified. To solve the polarization sensitivity of SiP photonic integrated circuits (PICs), in chapter 3 we improve our design by including polarization diversity. By introducing a new evaluation metric for quantifying the effect of frequency drift, comprehensive simulations provide a generic guidance on the MRR design and system operations to achieve the best performance in real engineering scenarios. In chapter 4 we discuss the overlay of 5G signal over PON. We experimentally demonstrate the simultaneous hybrid detection of traditional PON traffic and RoF signal while enabling the carrier remodulation for uplink. The conclusion of the thesis and the discussion of future work is included at the end of this thesis.

I.3.1 Objectives and contributions in Chapter 1

We experimentally demonstrate the generation of a single-sideband orthogonal frequency division multiplexed (OFDM) signal using an on-chip silicon photonics microring-based IQ modulator. Over 18 dB sideband suppression ratio is achieved for the wideband OFDM: 15.7 GHz data band and 2.7 GHz guard band. The 31.4 Gb/s signal is transmitted over 20 km of standard single-mode fiber with a bit error rate below the forward error correction threshold.

This chapter details the following main contributions:

- Generate single side band by IQ MRM
- Experimentally demonstrate the SSB transmission via 20 km fiber

I.3.2 Objectives and contributions in Chapter 2

The beat interference cancellation receiver was firstly demonstrated by Peng, Wei-Ren et al. [12] with discrete components. The drawback of complexity and cost of a discrete component solution limits the use of this SSBI cancellation scheme. We propose a compact integrated solution to eliminate SSBI by reconstructing SSBI. The SSBI reconstruction is achieved by

carrier suppression via MRR. We discuss the non-ideal filtering effect of MRR and introduced a scaling factor to balance the effect to optimize the performance. Trade-offs are made through simulation to provide a prediction on optimized settings. We demonstrate the DD-OFDM transmission system with different CSRs (from low value 0 dB to moderate one 5 dB). After SSBI cancellation we get uniformed high quality subcarrier performance even with 0 dB CSR. Different frequency offsets between the MRR resonance peak and carrier is explored to prove the robustness of our proposed solution. Good levels of performance are obtained for all CSR levels for a frequency offset range of 12 GHz.

This chapter details the following main contributions:

- Subsystem design for SiP SSBI cancellation.
- Description of non-ideal filtering and introduction of a scaling factor in balanced detection to combat this effect.
- Experimental validation of good SSBI cancellation performance under ultra low CSR.
- Experimental validation of performance robustness in the presence of frequency drift.

I.3.3 Objectives and contributions in Chapter 3

In the work described in the past chapter, we propose and experimentally demonstrate an SSBI cancellation subsystem based on SiP. In this chapter we improve the integration level by adding the polarization diversity and ability of realizing arbitrary splitting ratio. Then inspired by previous study on influence of non-ideal filtering effect, we explore more details in this chapter. We introduce a new performance metric, minimum guaranteed Q, to evaluate the SSBI cancellation performance against frequency drift. The spectral efficiency is maximized via the optimization of the controllable operation parameters. Finally, generic guidance is provided, including the MRR design as well as the controllable parameters to achieve the highest spectral efficiency.

This chapter details the following main contributions:

- Enhanced SSBI cancellation system with polarization diversity and on-chip scaling factor
- A new metric to evaluate the system performance under unstable frequency offsets
- Guidance on MRR designs and system operation parameters to optimize performance in practical application

I.3.4 Objectives and contributions in Chapter 4

In this chapter, we experimentally validate a silicon photonic subsystem designed for passive optical networks with carrier reuse. The subsystem enables radio-over-fiber signals to cohabit an assigned wavelength slot without perturbing the PON signal. The residual carrier is remodulated via a microring modulator for the RoF uplink. We successfully detected the dropped 8 GHz broadband signal and five 125 MHz radio-over-fiber signals while two 125 MHz radio over fiber signals are remodulated onto the carrier.

This chapter details the following main contributions:

- Propose a SiP system enabling hybrid detection of RoF and broadband signal
- Provide the carrier re-modulation functionality to generate uplink signal
- Experimentally validate the SiP transceiver

Chapter 1

Silicon Microring IQ Modulator Enabled Single-Sideband OFDM transmission

1.1 Résumé

La génération d'un signal de répartition multiplexée de fréquences orthogonales (OFDM) à bande latérale unique en utilisant un modulateur IQ sur puce basé sur le photonique au silicium à micro-anneau. Le ratio de suppression à bande latérale de plus de 18 dB est obtenu pour l'OFDM à large bande : bande de donnée de 15.7 GHz et bande de garde de 2.7 GHz. Le signal de 31.4 Gb/s a été transmis dans plus de 20 km de fibre de monomode standard avec un taux d'erreur sur les bits inférieur à la limite de la correction d'erreur sans voie de retour. Tandis que les signaux d'onde continue à bande latérale unique ont été produit avec un tel matériel, c'est la première démonstration de la stable transmission de données sur la porteuse à bande latérale unique.

1.2 Abstract

We experimentally demonstrate the generation of a single-sideband orthogonal frequency division multiplexed (OFDM) signal using an on-chip silicon photonics microring-based IQ modulator. Over 18 dB sideband suppression ratio is achieved for the wideband OFDM: 15.7 GHz data band and 2.7 GHz guard band. The 31.4 Gb/s signal was transmitted over 20 km of standard single-mode fiber with a bit error rate below the forward error correction threshold. While single-sideband continuous-wave signals have been produced with such hardware, this is the first demonstration of stable data transmission on the single sideband carrier.

1.3 Context and Contributions

This thesis covers the use of SiP subsystems for OFDM with direct detection, as well as SiP for 5G radio over fiber. In this chapter we demonstrate the generation of SSB OFDM over MRMs, while 5G radio over fiber is covered elsewhere.

The major contribution in this chapter is the experimental demonstration of a single sideband OFDM signal using an on-chip SiP MRM based IQ modulator. We generated a wideband OFDM signal with 15.7 GHz data band and 2.7 GHz guard band. The sideband suppression ratio is over 18 dB.

To exhibit the CD robustness, we demonstrated the transmission of 31.4 Gb/s SSB OFDM signal over 20 km of standard single-mode fiber. Without any extra CD compensation, the bit error rate is well under the FEC threshold.

We experimentally demonstrate the generation of a single-sideband orthogonal frequency division multiplexed (OFDM) signal using an on-chip silicon photonics microring-based IQ modulator. Over 18 dB sideband suppression ratio is achieved for the wideband OFDM: 15.7 GHz data band and 2.7 GHz guard band. The 31.4 Gb/s signal was transmitted over 20 km of standard single-mode fiber with a bit error rate below the forward error correction threshold.

1.4 Introduction

Passive optical networks (PONs) accomplish high-bandwidth Internet delivery by taking advantage of low loss optical fiber and simple on/off keying transceivers. As new video streaming and mobile services push the need for greater PON bandwidth, we need cost-effective hardware to work with advanced modulation to increase throughput. That modulation should remain compatible with simple direct detection schemes currently in use. The point-to-multipoint PON architecture provides an efficient access network that could be complemented with emerging silicon photonic components.

The major short-reach PON constraints are implementation cost and flexibility. Orthogonal frequency division multiplexing (OFDM) is attractive for PONs owing to its flexibility in sculpting both time and frequency resources. To maintain low cost and simplicity, direct detection (DD) OFDM is widely considered for future PONs [3]. Link performance is limited by chromatic dispersion (CD), which results in destructive interference between two sidebands of double sideband (DSB) OFDM modulation. It causes severe frequency-related power fading, especially for wider band signal and longer distances [13]. Single sideband (SSB) OFDM modulation avoids the power fading and doubles the potential spectral efficiency. SSB-OFDM modulation can be realized by directly filtering the undesired sideband [14], but requires sharp filters with well controlled center frequency to isolate one sideband precisely. External modulators [15], such as dual-drive Mach-Zehnder modulators (MZM) and optical in-phase and

quadrature (IQ) modulators, can generate SSB signals. Integrated versions of these modulators provide a more affordable solution.

Silicon photonics (SiP) is a CMOS-compatible technology based on high-index-contrast waveguides, that can be used for high-speed optical modulators [16]. Compared to MZMs, microring modulators (MRMs) [17] have the advantage of ultra-small footprint and low power consumption (down to fJ/bit), both superb attributes for short-reach applications. A microring IQ modulator was demonstrated for QAM modulation with coherent detection [18]. Single-sideband OFDM (with waterfilling) was experimentally demonstrated in [19] using a silicon IQ MZM. A single-chip MRM based optical SSB modulator was demonstrated in [20], but only for sinusoidal signals. Wideband SSB-OFDM transmission using an MRM, to the best of our knowledge, has not been reported until this time.

In this letter, we use a silicon microring IQ modulator to generate an optical SSB signal for a direct detection system. We demonstrate the generation of flat, wideband (15.7 GHz) SSB-OFDM with a 2.7 GHz guard band for a total covered bandwidth of 18.4 GHz. The sideband suppression ratio is larger than 18 dB. Transmission over a 20 km standard single mode fiber (SSMF) is presented, with a measured bit error rate well below the 7% overhead forward error correction (FEC) threshold. We discuss how this subsystem could enable upgraded data rates, as well as new services for PON systems.

1.5 Device Design and Characterization

We designed a microring IQ modulator on the silicon-on-insulator (SOI) platform. As shown in Fig. 1.1, two identical MRMs modulators (MRM1 and MRM2) are loaded in a balanced Mach-Zehnder interferometer (MZI). The $\pi/2$ phase shift between the branches allows operation of the modulators for complex (IQ) modulation. The phase shift tuning is implemented by a $100\ \mu\text{m}$ N⁺⁺/N/N⁺⁺ resistor-based heater.

Each MRM has a radius of $20\ \mu\text{m}$, a coupling gap of 180 nm, an all-pass structure and are over-coupled. They exploit the plasma dispersion effect through carrier depletion in a lateral p-n junction. The p-n junction for intracavity modulation spans roughly 70% of the circumference, whereas the N⁺⁺/N/N⁺⁺ resistor-based heater for wavelength tuning spans roughly 20% of the circumference, as shown in the partial mask layout in Fig. 1.2a. The cross

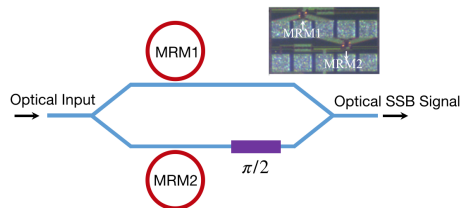


Figure 1.1: Schematic and microscope image of an optical SSB transmitter based on silicon microring IQ modulator.

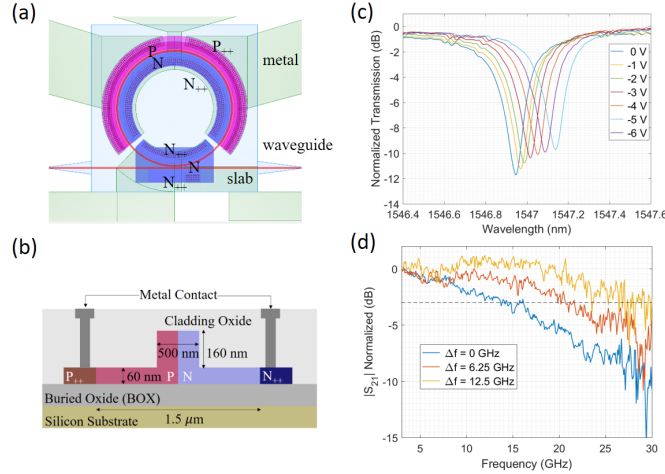


Figure 1.2: (a) Partial mask layout for MRM1/MRM2, (b) cross section of the p-n junction of MRM1/MRM2 showing relevant dimensions, for MRM1 measured (c) power transmission spectra at different bias voltages, and (d) electro-optic frequency response (S_{21}) at different frequency detunings.

section of the waveguide phase shifter is shown in Fig. 1.2b. The silicon waveguide has a rib thickness of 220 nm with a 60 nm thick slab used for electrical connections. The device was fabricated in a multi-project-wafer run at IMEC, Belgium. Bond pad for RF probing dominate the $0.69 \text{ mm} \times 0.41 \text{ mm}$ footprint.

The measured optical transmission spectra of MRM1 for various bias voltages are presented in Fig. 1.2c. The MRM exhibits a resonance depth of around 10.8 dB at zero bias. The depth decreases as the reverse potential increases, indicating an over-coupling condition in reverse bias. The resonance shift as a function of reverse bias voltage shows an efficiency of about 2 GHz/V. The measured free spectral range (FSR) is 4.78 nm and the quality factor at equilibrium is 8320. Frequency detuning Δf , defined as the difference between the optical input frequency and the cavity resonant frequency. The measured MRM1 electro-optic, S_{21} , response at -2 V bias is reported in Fig. 1.2d for various detunings; 3 dB bandwidth is greater than 25 GHz at -2 V bias for 12.5 GHz detuning.

1.6 Experimental Setup

The experimental setup is illustrated in Fig. 1.3. The Cobrite external cavity laser (100 kHz linewidth) was tuned to 1550.5 nm and coupled to the chip with a $250 \mu\text{m}$ spaced fiber array via polarization maintaining fiber. A 23-order pseudo random bit sequence (PRBS) was mapped to QPSK and OFDM coded (details in next section). Only positive subcarriers (higher frequency than the optical carrier) are non-zero, i.e., single-side-band OFDM in the electrical domain. The OFDM IQ values are fed to two channels of an 84 GS/s digital-to-analog converter (DAC) with 16 GHz bandwidth and 8-bit resolution. The driving signals generated by the DAC are amplified by two cascaded 50 GHz RF amplifiers.

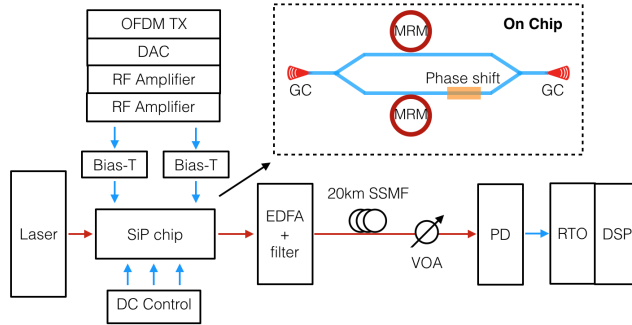


Figure 1.3: Experimental setup

The two MRMs on chip are driven via a GSGSG configured, $50\ \Omega$ -terminated, 50 GHz micro probe. The two rings are heated to change the offset between the resonance peak and laser wavelength. The waveguide in the lower branch of the MZI is also heated to generate a 0.5π phase difference between the two arms of the IQ modulator with a DC driving voltage of ~ 1.3 V. An EDFA boosts chip output power. A tunable optical band pass filter (OBPF) with a 0.4 nm passband bandwidth removes out-of-band amplified spontaneous-emission noise. After 20 km SSMF propagation, a variable optical attenuator (VOA) sweeps received power to a photodetector with a transimpedance amplifier. The electrical signal is captured at 80 GSa/s by a real-time oscilloscope (RTO) with 30 GHz analog bandwidth.

1.7 Experimental Results

1.7.1 Generated SSB-OFDM signal

The OFDM signal is generated off-line in Matlab. The IQ modulator uses complex data to produce a single sideband version in the optical domain. The dark grey curve in Fig. 1.4 shows the optical spectrum of the SSB-OFDM signal before transmission. The left sideband is well suppressed by IQ modulation, with sideband suppression ratio greater than 18 dB. The OSNR is limited by electrical driving signals. The cascaded amplifiers are sub-optimal, but required due to equipment availability. The weak DAC electrical output (50 mV peak-to-peak amplitude) was amplified to $5\ V_{pp}$. The degraded electrical SNR leads to an OSNR of approximately 18 dB. The residual sideband is almost totally buried by the noise. Small distortions near the carrier and after the OFDM band are due to DAC imperfections.

The data was QPSK modulated and parsed into blocks of 191 symbols. The symbols were zero padded to form a block of length 1024, corresponding to the total number of subcarriers. The FFT length of 1024 covers 84 GHz (DAC sampling rate of 84 GS/s), for a subcarrier bandwidth of 82 MHz. The suppressed sideband is a result of the 512 lower subcarriers being zeroed out. We allocated 33 subcarriers (2.7 GHz) as a guard band, so the 191 data subcarriers (15.7 GHz) were followed by 288 zero subcarriers at the highest frequencies. The guard band avoids severe signal-to-signal beat interference (SSBI) at baseband; for more spectral efficiency,

a Kramer-Kronig receiver[21] could be used without a guard band.

The upper frequencies were unused due to the bandwidth of the MRMs. Per measurements in Fig. 2, the 3 dB bandwidth of the MRM is around 23 GHz. A section of 6.25% of the signal was appended as a cyclic prefix to increase the dispersion tolerance. Linear pre-emphasis was used to balance the non-flat DAC response, and uniform subcarriers are observed in the optical spectrum in Fig. 1.4. The slight notch comes from the imperfect DAC frequency response, which leads to the poor performance of the middle subcarrier to be seen later in Fig. 1.6.

In [20], a single sideband sinusoidal signal is presented within a 5 GHz range, so wideband modulation of the sideband was not examined. The MRM has inherent frequency selectivity. On the positive side, we can cascade ring-based IQ modulators to realize modulation of wavelength division multiplexing (WDM) signals without additional filters as discussed in section V. However, at the same time, the MRM filtering effect imposes a frequency roll-off on the modulated signal. As the overall performance of OFDM transmission is limited by the worst subcarrier, it is important to maintain uniform performance of all subcarriers. In wide-band signal generation, the roll-off will result in worse performance for higher frequency components. To compensate the response of MRMs, pre-emphasis can be used to balance the subcarrier performance. However, too strong pre-emphasis degrades the overall performance, ultimately limiting bandwidth.

Fig. 1.5 shows the received electrical spectrum after 20 km SSMF transmission. In Fig. 1.5a the transmitted signal was SSB-OFDM with spectrum in Fig. 1.4. In Fig. 1.5b the transmitted signal was instead DSB-OFDM signal with the same number of subcarriers and guard band. For both cases, the received power is adjusted to -1 dBm using a VOA. The advantage of SSB modulation is clearly visible: the SSB-OFDM signal shows a flat spectrum, while the DSB-OFDM signal has severe attenuation in frequencies near the optical carrier due to the chromatic-dispersion-induced nonlinear phase response. This results in strong fading of DSB-OFDM after direct detection. An inset shows the constellation of the last subcarrier for each case. The DSB-OFDM constellation is noisier than the SSB-OFDM signal due to interference.

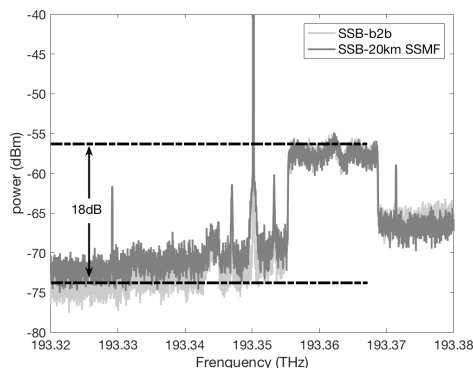


Figure 1.4: Optical spectrum of SSB-OFDM signal before transmission in dark grey and after 20 km transmission in light grey.

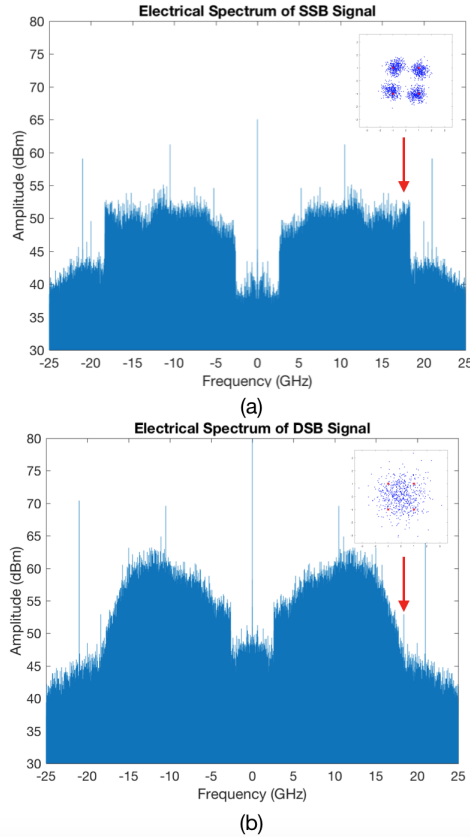


Figure 1.5: Received electrical spectrum and constellations for after transmission over 20 km of SSMF of (a) SSB-OFDM signal of Fig. 1.4, and (b) a DSB-OFDM signal; insets show constellation of subcarrier number 191.

As ring modulators are resonant structures, phase shift is frequency dependent. The single phase compensation for the whole band leads to residual phase shift at the last subcarrier, hence the visible constellation rotation.

1.7.2 BER performance

We generate a PRBS sequence off-line in Matlab. The sequence is mapped on 191 subcarriers to generate 10,000 QPSK OFDM symbols per frame. Zeros are padded to form the final frame with a length of 2^{22} . In each detection, the frame is captured five times and the counted errors are averaged for higher precision.

We find the BER performance for DSB and SSB signals to highlight the improvement with efficient SSB generation. We calculate the BER per subcarrier; frequency-dependent impairments are clearly eliminated with SSB. We estimate SNR from BER and plot the estimated SNR per subcarrier in Fig. 1.6. Performance is uniform over all subcarriers after the 20 km SSMF in the solid (blue) curve for SSB-OFDM in Fig. 1.6. The small notch comes from DAC imperfections for both SSB and DSB signal. The overall estimated BER is 2.75×10^{-3} , well below the 7% FEC threshold (3.8×10^{-3}). In the dashed (red) curve for DSB-OFDM in Fig. 1.6 we can see clear fading due to chromatic dispersion. As the overall performance is

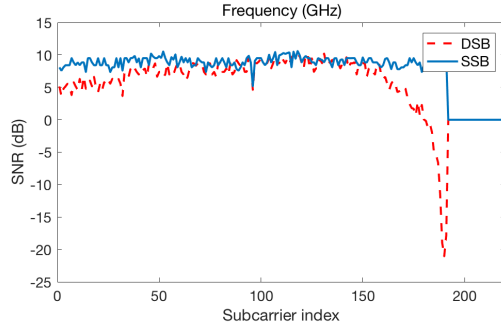


Figure 1.6: Estimated SNR per subcarrier for SSB signal (solid blue curve) and DSB signal (dashed red curve)

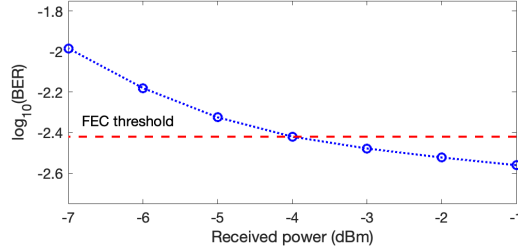


Figure 1.7: BER of detected SSB-OFDM signal with varied received power.

dominated by the worst subcarriers, the performance of DSB sees a significant degradation; the overall counted BER for DSB-OFDM is 2.6×10^{-2} .

The transmission performance of SSB-OFDM signal over a range of receiving power is shown in Fig. 1.7. We use the 7% FEC threshold as a reference. The BER increases smoothly as the received power drops. For a received power larger than -4 dBm, we achieve error-free transmission.

The optical spectrum of the generated SSB-OFDM signal after 20 km SSMF is shown in the dark grey curve in Fig. 1.4. The spectrum remains uniform after transmission while the left side band is totally buried by the noise. The OSNR decreases due to the fiber loss, which limits the performance. The OSNR in this demonstration is limited by the poor electrical signal quality. Better performance can be achieved with a higher output power DAC or low-noise RF amplifiers.

1.7.3 Discussion

MRMs are inherently frequency selective. Using MRMs at the customer premises could enable WDM on current PON infrastructures without deploying array waveguide gratings (AWGs). A colorless solution [22] could be achieved by tuning the MRM center frequency at the customer premises.

MRMs could also be effective at the central office for generation of WDM signals. Both paths of the IQ modulator could incorporate multiple MRMs in a cascade sharing the same single bus. With a comb source input, different sets of MRMs can be thermally tuned to the frequencies of the comb lines and modulate the tones. As shown in Fig. 2, the bandwidth

of the MRM is around 0.2 nm, significantly smaller than the typical WDM grid (0.8 nm). Cascaded MRMs can be tuned to create 0.8 nm frequency drift between adjacent MRMs. For every set of MRMs, only one tone is modulated; other tones, as well as the modulated signal (within 0.2 nm range to tones), are out of band and unaffected.

MRMs could also enable new PON services. By designing MRMs with higher Q factors, we can realize very narrow bandwidth MRMs to support radio over fiber (RoF) multiplexing. An MRM with confined operation bandwidth allows us to add several downlink RoF channels onto tightly spaced wavelengths falling within a single WDM slot. Single sideband RoF signals could be generated via the IQ structure to achieve a doubled spectral efficiency and thus higher flexibility in wavelength. While MRMs are sensitive to fabrication tolerance and environmental temperature, this can be addressed using feedback control [23].

1.8 Conclusion

We demonstrated, for the first time, the generation of wide-band optical SSB-OFDM over a 15.7 GHz bandwidth with a 2.7 GHz guard band, using an integrated silicon microring IQ modulator. The side-band suppression ratio is 18 dB over a wide range. Performance and robustness against chromatic dispersion is examined via transmission of 20-km SSMF. A raw data rate of 31.3 Gb/s with a 6.25 % cyclic prefix has been achieved. This subsystem provides a low-cost integrated solution for SSB signal transmitters. The frequency selectivity and tunability allows colorless operation in next-generation PONs. This solution is also compatible with WDM without additional equipment such as wavelength (de-)multiplexers.

Chapter 2

SiP-based SSBI Cancellation for OFDM

2.1 Résumé

Nous proposons pour la première fois d'utiliser une solution de photoniques au silicium (SiP) pour un réseau optique passif afin de réduire les interférences de battement signal-signal (SSBI) et de récupérer une partie de la porteuse de liaison descendante pour une utilisation dans la liaison montante. Le récepteur Kramers-Kronig (KK) pour la détection directe des formats de modulation avancés surmonte SSBI au prix d'un ratio porteuse/signal modéré (> 6 dB) et du suréchantillonnage élevé ($4 \times$). Nous proposons une solution SSBI optique qui obtient de meilleures performances que KK et ne nécessite qu'un échantillonnage standard et un bas (3 dB) ratio de puissance porteuse/signal. Le récepteur est conçu pour la liaison descendante dans les réseaux optiques passifs, où la porteuse du signal doit être économisée pour la réutilisation dans la liaison montante. En utilisant la SiP d'un bon rapport coût/efficacité et à faible consommation d'énergie, le récepteur filtre le signal entrant, supprime la SSBI et achemine une partie de porteuses pour une utilisation dans la liaison montante.

Nous examinons expérimentalement la suppression SSBI dans cet article. Tandis que les démonstrations précédentes utilisaient des composants encombrants et discrets, nous obtenons une amélioration significative du facteur-Q avec une solution SiP simple. Nous examinons le décalage de fréquence optimal entre la porteuse et la fréquence centrale du résonateur micro-anneau. La robustesse contre la dérive de fréquence, de même que l'impact d'un filtrage imparfait, est discutée et quantifiée.

2.2 Abstract

We propose for the first time to use a silicon photonics (SiP) solution for a passive optical network to both reduce signal-signal beat interference (SSBI) and recuperate a part of the downlink carrier for use in the uplink. The Kramer-Kronig (KK) receiver for direct detection of advanced modulation formats overcomes SSBI at the cost of a moderate carrier to signal ratio (>6 dB) and high oversampling ($4\times$). We propose an optical SSBI solution that achieves better performance than KK and requires only standard sampling and low (3 dB) carrier to signal power ratio. The receiver is conceived for the downlink in passive optical networks, where carrier signal must be husbanded for re-use in the uplink. Using cost effective and power efficient SiP, the receiver filters the incoming signal, suppresses SSBI, and routes a portion of the carrier for use in the uplink.

We experimentally examine the SSBI suppression in this paper. While previous demonstrations used bulky, discrete components, we achieve significant Q-factor improvement with a simple SiP solution. We examine the optimal frequency offset between the carrier and the microring resonator center frequency. The robustness to frequency drift, as well as the impact of imperfect filtering, is discussed and quantified.

2.3 Context and Contributions

This thesis covers the use of SiP subsystems for OFDM with direct detection, as well as SiP for 5G radio over fiber. In this chapter and the next we look at SSBI suppression for OFDM, while 5G radio over fiber is covered elsewhere.

The major contribution in this chapter is a subsystem design in SiP which had previously only been accomplished in discrete components. This subsystem can cancel SSBI by recreating the interference and subtracting it via balanced detection from the data signal corrupted with SSBI.

As our SiP solution cannot filter the signals ideally, we examine a scaling factor to be introduced to the balanced detection that can trade-off the non-ideal filtering effects. In our experiment we show the interference is cancelled allowing good performance even when the carrier is weak, that is, for ultra low CSR of 0 dB.

Although our SiP MRRs are sensitive to temperature effects, our experimental demonstration shows the tuning of the resonant frequency can drift by as much as 12 GHz from the targeted value, and still provides good performance.

2.4 Introduction

Coherent detection has whetted our appetite for higher bandwidth communications, but we also crave the low cost of direct detection. One solution for high bit rate with direct detection is the use of optical orthogonal frequency division multiplexed (OFDM) with a distributed carrier; however, performance is limited by signal to signal beat interference (SSBI). Quadrature amplitude modulation (QAM) or OFDM can also be achieved with direct detection when using the Kramer-Kronig (KK) receiver. We propose a simple, integrated subsystem that can suppress SSBI in OFDM, without the DSP and high oversampling required for KK reception.

Optical OFDM is a promising solution for passive optical networks (PONs), as it is particularly flexible in sculpting both time and frequency resources. To avoid fading that is induced by chromatic dispersion [24], PONs could use single side-band (SSB) OFDM. As PONs require low cost user equipment, direct detection (DD) of optical OFDM is the preferred solution. In direct detection, beating between signal and carrier generates the desired OFDM signal, however, beating among the OFDM subcarriers (signal-to-signal beat interference or SSBI) obscures the desired part of the electrical spectrum. It is the major source of impairment in DD-SSB-OFDM systems.

There are several approaches to deal with SSBI in digital signal processing. Most recently linearization filtering is used, whereby the SSBI is estimated from the received signal and subtracted before data detection [25; 26]. These approaches exploit the deterministic nature of SSBI, and have been applied to discrete multi-tone (a variety of OFDM) [25] and QAM modulation [26; 27; 28]. An experimental comparison in [21] concluded that the KK DSP method yielded better performance than DSP linearization.

All direct detection solutions, whether OFDM or QAM, optical or digital SSBI suppression, use a carrier stronger than the signal to enhance reception. In KK the carrier to signal ratio (CSR) should be above 6 dB for bit error rate (BER) on the order of 10^{-2} with 6-8 samples per symbol.[29]. Upsampling (after reception at the standard two samples per symbol for SSB-OFDM) is required due to the square-root and logarithm operations in KK. There have been many examinations of the effect of CSR and upsampling rate on BER for KK. The performance falls off precipitously for CSR below 6 dB, and severe penalties are incurred for moderate upsampling ($2.5-3\times$) [30].

Several solutions have been proposed to enhance KK, including an optical sub-assembly whose complexity is similar to that in this paper [31]. Using this optical sub-assembly for KK, the sampling rate was reduced to the standard two samples per symbol and BER $\sim 10^{-2}$ was achieved at CSR of 3 dB. However, additional DSP was required, as well as the optical sub-assembly; a gradient descent optimization in DSP involved thousands of iterations.

We propose for the first time to use a SiP solution to both reduce SSBI and recuperate a

part of the downlink carrier for use in the uplink. In cost-effective, single-feeder PONs, the carrier is reused for uplink modulation to achieve colorless operation. Methods using high CSR are not suitable in these PONs. The carrier reuse limits the CSR power budget. The portion of carrier power reserved for direct detection may not be sufficient to meet the KK carrier amplitude requirements, i.e., minimum phase. This is particularly true for KK receivers for OFDM, whose greater peak to average ratio would require even greater CSR than that reported when using QAM modulation with KK.

We address the significant challenge in working with low-cost SiP filtering for SSBI cancellation. We focus on the microring resonator (MRR) structure for the SSBI suppression on the through port, as the MRR can also provide downlink carrier recovery on the drop port. In this paper we focus on the through port filtering performance, which must be designed for robustness against temperature induced frequency drift. We examine experimentally an MRR subsystem designed for both SSBI cancellation and carrier reuse.

We first discuss the details of the fabricated integrated SSBI cancellation subsystem in section II. In section III we examine the non-ideal filtering effect that could undermine the cancellation performance. System simulation were completed to predict the performance. In section IV we discuss the design and characterization of the micro ring resonator for carrier suppression. After a description of the experimental setup, performance improvement using SiP SSBI cancellation system is evaluated experimentally. Several optimal choices for the system operating point are identified.

2.5 System Design

Optical SSBI cancellation in OFDM is both 1) appropriate for PONs and 2) high performance. In these approaches, optical signal processing creates a copy of the SSBI. The SSBI signal is isolated optically, photo-detected, and its electrical version is subtracted from the photo-detected signal corrupted by SSBI; the resulting signal is free of SSBI. This has been examined analytically [9] and experimentally using discrete components [10].

The only experimental optical approaches for SSBI cancellation in the literature have had high system complexity due to the use of discrete components. We examine the use of silicon photonics to overcome this limitation. We propose an integrated SSBI cancellation subsystem in SiP to avoid drawbacks of using discrete components. We demonstrated the first proof-of-concept for silicon photonics (SiP) SSBI cancellation at Microwave Photonics Conference 2017 [32] using micro ring resonators (MRRs). That demonstration used cascaded MRRs, whose low extinction ratio and wide bandwidth limited the SSBI cancellation.

In Fig. 2.1 we illustrate SSBI cancellation in the the optical domain proposed by [9]. The signal with mixed polarization (frequency domain rectangle with gradient fill) is sent to a

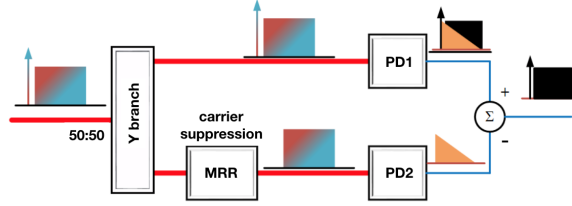


Figure 2.1: Optical SSBI cancellation scheme with ideal carrier suppression

power splitter, i.e., y branch. One is directly sent for detection, where we will get the detected signal as well as SSBI. The other path is sent to a filter that suppresses the carrier, but passes the data. Without the carrier, i.e., with ideal carrier suppression, we detect the SSBI alone. By subtracting the SSBI from the through path output, we can realize SSBI cancellation.

The discrete component approach is limited by excessive losses and by unequal delays which are difficult to equalize (keeping the two paths exactly the same length). Therefore, we turn to integrated solutions to avoid those drawbacks. The frequency response of the MRR to suppress the carrier is a notch. Ideally, we suppress the carrier and leave data unchanged [33]. The Y branch is used to split the light into two paths. A polarization controller is required, as generally SiP components are sensitive to polarization, while the light coupled into the chip arrives with an arbitrary polarization state. Integration ensures that 1) all paths are produced with similar lengths, 2) any environmental changes are experienced simultaneously on all components, and 3) cost is low and footprint is small. As the optical path on-chip is only several millimetres, the fabrication mismatch of the two paths will be negligible.

The hardware requirements for optical SSBI cancellation call for an additional photodetector vis-a-vis a conventional receiver with digital SSBI cancellation. However, digital processing alone approaches (including the KK receiver) require at least moderate CSR. We will show optical signal processing can suppress SSBI even at 0 dB CSR. To lower the minimal KK CSR (~ 6 dB), an enhanced KK receiver was proposed in [31]. For enhanced KK, the signal is split into two branches, as in our solution. Dispersive material is used to differentiate the two branches, and then the standard KK procedure is applied to both branches. With an additional gradient descent algorithm in DSP, the performance can be optimized to reduce required CSR by 3 dB. This reduction is still not as great as the one we demonstrate with optical SSBI suppression. In addition, we avoid the DSP costs (high iterations of the gradient descent algorithm) in the enhanced KK receiver. Our proposed subsystem is a better solution when low CSR is critical, as in a PON that reuses the carrier for the uplink.

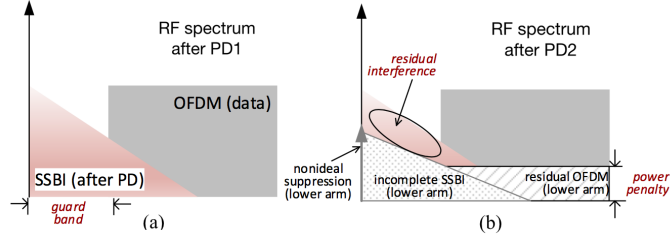


Figure 2.2: Non-ideal filtering effect

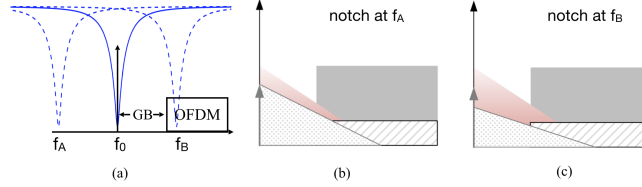


Figure 2.3: a) Carrier and OFDM placement vis-à-vis offsets. Electrical spectrum components for different cases of frequency offset, b) notch at carrier, c) notch more distant from OFDM signal, and d) notch closer to OFDM signal

2.6 The Effect of Non-ideal Filtering Effect

In this section we examine the impact of imperfect filtering on the SSBI cancellation efficiency. Two factors enter into consideration: 1) the finite roll-off of the filter, and 2) the frequency offset of the carrier from the notch center frequency. We examine via simulation the impact of the first as a function of κ (the coupler design of the MRR) and the second as a function of the detuning between signal and filter. In later sections we will confirm our simulation results experimentally.

2.6.1 Spectral effects

An illustration of the electrical spectrum after PD1 (from Fig. 2.1) is shown in Fig. 2.2a; it consists of the desired OFDM signal (rectangular) and the SSBI (triangular). Fig. 2.2b shows the electrical spectrum at PD2 in hashed regions, superimposed on Fig. 2.2a spectrum. Although the carrier is located exactly on the notch, the effect of a non-ideal frequency response, $H(f)$, is visible: there is a residual carrier and thus residual OFDM. After subtracting the RF spectrum at PD2 from the RF spectrum at PD1, these residuals result in a power penalty. Because the OFDM signal sees non-flat frequency response, the SSBI reconstruction is also incomplete at PD2. This causes incomplete SSBI cancellation.

As the filtering effect can arise from center frequency offset, consider three frequency offset scenarios shown in Fig. 2.3a: no frequency offset, offset f_A to frequencies far from the OFDM signal, offset f_B to frequencies close to the OFDM signal. When there is no frequency offset, the RF output spectra are shown in Fig. 2.2b. The carrier sees maximum suppression, and

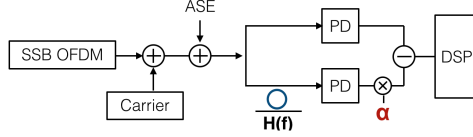


Figure 2.4: Simulation system setup

the OFDM band suffers limited filtering effects.

When the notch is at f_A , the RF output spectrum, shown in Fig. 2.3b has a prominent carrier and the OFDM band is little changed. The presence of the carrier leads to residual OFDM at PD2, hence a greater power penalty. The SSBI reconstruction is improved since the OFDM signal was less distorted by $H(f - f_A)$. These two opposite influences will moderate the overall performance, and may even lead to better performance for this type of offset.

When the notch is at f_B , the RF output spectrum is as illustrated in Fig. 2.3c. As with case f_A , there is a prominent residual carrier; case f_A and f_B see the same increased power penalty. The OFDM band, however, sees much stronger filtering than either case f_0 or f_A . This leads to worse SSBI reconstruction, thus the performance will drop fast.

2.6.2 Simulation setup

We investigate the non-ideal filtering effect with the simulator model illustrated in Fig. 2.4. We generate 16 Gbaud QPSK single side-band OFDM signal over 256 subcarriers. We do not use a guard band. We add a carrier to achieve 5 dB CSR. Amplified spontaneous emission (ASE) noise in the form of additive white Gaussian noise is added to adjust the optical signal to noise ratio (OSNR) to 25 dB. To emulate the optical SSBI cancellation procedure, we divide the signal into two parts with equal power. One part is directly detected by a square law PD. The other part is filtered by a MRR to suppress the carrier. The MRR frequency response, $H(f)$, is simulated using the transfer matrix method. Various coupling coefficients κ , the coupling coefficient of the bus-resonator coupler, are examined. After carrier suppression, the reconstructed SSBI is used to cancel SSBI in the through path.

For each subcarrier we count errors, N_{err} , over the 10^5 symbols transmitted. We also calculate average error vector magnitude (EVM) for the QPSK constellation. To improve accuracy [34], we estimate bit error rate (BER) from both counted errors and the average EVM per

$$BER = \begin{cases} N_{err}/10^5 & \text{for } N_{err} \geq 10 \\ \frac{1}{2} \text{erfc}(1/\sqrt{2}EVM) & \text{for } N_{err} < 10 \end{cases} \quad (2.1)$$

where the erfc is the complementary error function. The Q-factor for QPSK is found from the

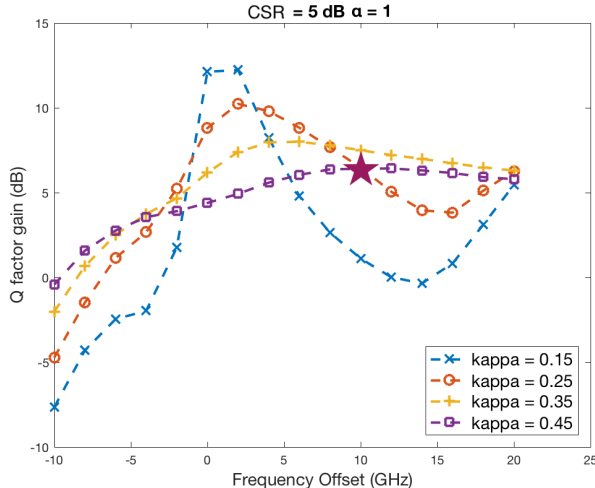


Figure 2.5: Simulation of SSBI cancellation performance via different frequency offsets ($\alpha = 1$)

estimated BER per

$$Q = \sqrt{2} \operatorname{erfc}^{-1}(2BER) \quad (2.2)$$

The Q-factor gain after SSBI cancellation with different frequency offsets is shown in Fig. 2.5. Very negative frequency offset sees little improvement, and in fact, sees mostly negative Q-factor gain, i.e., worse performance. This confirms our discussion of the scenario in Fig. 2.2c. As frequency offset approaches zero, we are more likely to see positive gain, again matching our discussion in the previous section, this time for the scenario in Fig. 2.2b. For positive frequency offset, the trade-off between non-ideal carrier suppression and undesired filtering on OFDM will give us a sweet spot that is highly dependent on MRR design.

2.6.3 Scaling factor α

The original SSBI cancellation calls for subtraction of the two photodetector outputs. We introduce a new parameter, scaling factor α , to create a scaled SSBI estimate. Given the competing contributions of imperfect filtering, it is possible that we can improve performance by subtracting a scaled version of the SSBI estimate. For this reason, we examine the use of α in the MRR branch after photodetection. This additional degree of freedom could counter-balance, to some extent, the variation in Q-factor due to frequency offset. We note in passing that the linearization filter method as well as enhanced KK receiver used a parameter similar to α to optimal SSBI estimation.

We sweep the α from 0.1 to 1.5 with a step of 0.1. The point ($\kappa = 0.45$, 12 GHz offset) marked with a star in Fig. 2.5 is the one detailed in Fig. 2.6. The blue curve in Fig. 2.6, no SSBI

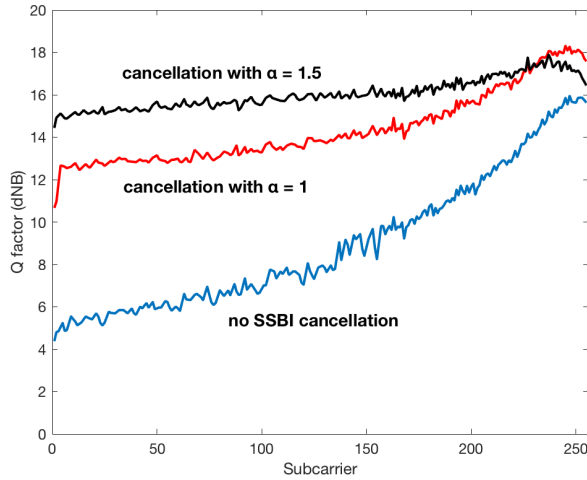


Figure 2.6: Simulation of Q-factor per subcarrier with varying α for $\kappa = 0.45$ and 10 GHz frequency offset

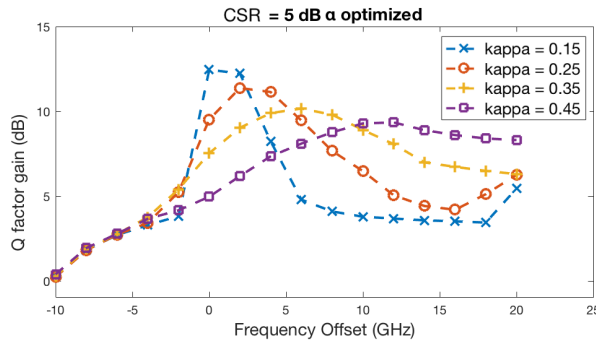


Figure 2.7: Simulation of SSBI cancellation performance via different frequency offsets (α optimized)

cancellation, has lower-index subcarriers suffering stronger SSBI; the Q-factor increases as the subcarrier index increases. For SSBI cancellation with $\alpha = 1$, red curve, the performance per subcarrier is more uniform. Due to the incomplete SSBI cancellation, the lower-index subcarriers still perform worse than others. The best overall SSBI cancellation is found for $\alpha_{opt} = 1.5$, black curve. The performance is much more uniform across carriers. Gains in lower-index subcarriers translate to overall improvement despite a small dip in performance at the highest index subcarriers.

In Fig. 2.7 we recreate the Q-factor gain from Fig. 2.5, but this time using the optimal alpha (a different α for each data point). Comparing Fig. 2.5 with Fig. 2.7, we avoid degraded performance. Considering all κ simulated, positive gain can be increased by 1.2 dB on average. In general, the gain improves most for larger κ . For $\kappa = 0.45$, the positive gain increases by 2.01 dB on average, with a maximum increase of 2.92 dB. While there is some improvement in

the maximum Q-factor gain vs. frequency offset, the frequency offset yielding the maximum Q-factor gain appears unchanged with α .

2.6.4 MRR design trade-offs

As shown in Fig. 2.7, the maximum Q-factor gain occurs at an offset that varies with κ , that is, a given frequency response $H(f)$ will lead to a different optimal offset. The best achievable performance for certain MRR designs occurs at small positive frequency offset, which means that the OFDM signal and carrier fall on the edge of the MRR response. By changing the scaling factor, we can keep the roll-off of a given choice of κ , but adjust the impact at a particular frequency. Working only with adjusting κ would require us to change the roll-off and therefore induce undesired affects at other frequencies.

For instance, if we tried to use a smaller κ , we would necessarily see a smaller extinction ratio, smaller full wave half maximum (FWHM) bandwidth and sharper roll-off, which would provide carrier suppression without much undesired filtering on the signal band. However, due to the small FWHM, the range in which we could suppress the carrier is also smaller. More precise wavelength control is also required for smaller κ MRRs. When trying larger κ , the roll-off is shallower, and we will suffer more undesired signal filtering, in order to achieve more carrier suppression. The tolerance to frequency drift will improve. Though not shown in the simulation, there is a limit to moving to smaller coupling ratio. A minimum extinction ratio is needed to achieve sufficient carrier suppression.

2.7 Experimental Results and discussion

Our first proof-of-concept experiment using silicon photonics cascaded microring resonators for SSBI cancellation was presented at MWP 2017 [32]. We present in this paper improved results using a notch shaped response in a single MRR. We first characterize the fabricated MRR. Then the subsystem, Y branch and MRR, is demonstrated experimentally.

2.7.1 Design and characterization of MRR

The new MRR consists of two straight waveguides and a single ring between them. The ring radius is $44.8 \mu\text{m}$ for a resonance peak near 1550 nm and free spectral range around 2 nm . The width and height of the waveguide are 500 nm and 220 nm respectively. The gap between the ring and straight waveguides is 200 nm on both sides. The coupling length of the directional coupler is $8 \mu\text{m}$. The SiP chip is fabricated using a 220-nm silicon-on-insulator (SOI) process through the CMC Microsystem SiP MWP service. The lithography of the fabricated chip is at 193 nm .

We use a 25° fiber array to couple light into the chip to characterize our design. The coupling loss is around 15 dB . We sweep the laser frequency, and measure the power output to estimate

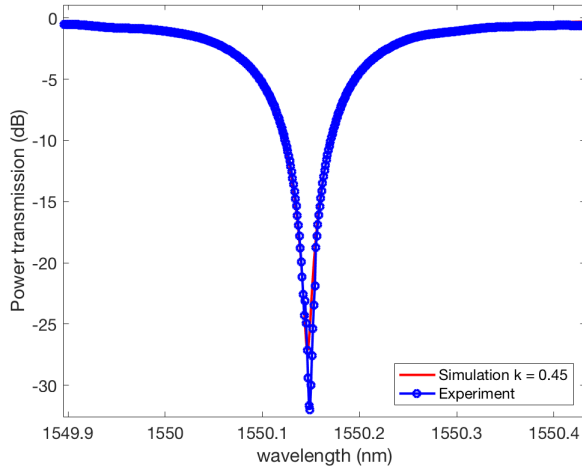


Figure 2.8: Characterization of new MRR

the frequency response. After compensating for coupling loss, we fit the frequency response curve to simulated ones based on our design parameters. The simulated response of the two bus MRR is found using the transfer matrix method [35]. The ring radius and coupling length are set to design parameters, while the coupling coefficient κ is fitted, as described in the following. The coupling loss is assumed to be 3 dB/cm.

Due to fabrication errors, the central frequency and the response shape may vary from chip to chip. The blue curve with circle markers in Fig. 2.8 represents the measured response of the MRR used in experiments reported in the next section. We neglect the coupling loss in our simulations. We shift the measured central frequency to match the design target, i.e., the simulated central frequency. For $\kappa = 0.45$, we obtain the red curve (no markers) in Fig. 2.8. When testing five fabricated chips, the estimated coupling coefficient κ varied from 0.36 to 0.46. The extinction ratio is larger than 30 dB, and the full width half maximum (FWHM) bandwidth is around 18 GHz for the MRR used in the experiment reported in the next section.

For comparison, the third-order MRR used in [32] had a radius of 10 nm for each of its three component rings. The asymmetric coupler gap was 150 nm, while the gap between the rings are 180 nm. The coupling length of the directional coupler was 6 μm . Three resonance peaks were observed in every period. Two resonance peaks were used to as carrier suppression filters in that experiment. One had 17 dB extinction ratio and FWHM bandwidth is around 43.5 GHz. The other had an extinction ratio around 12 dB and FWHM around 25 GHz.

2.7.2 Experimental setup

Fig. 2.9 shows the experimental setup. A single-side-band OFDM signal, with 16 GBaud bandwidth, 256 subcarriers, and without guard band, is generated offline with MATLAB. The electrical QPSK signal is generated by a 64-GS/s digital-to-analog converter (DAC) with

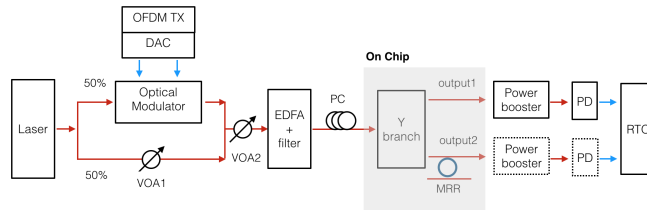


Figure 2.9: Experimental Setup; as identical photodetectors were not available, a single photodetector is time multiplexed

15 GHz bandwidth and 8 bit resolution. The signal drives an SHF IQ modulator whose input is a laser with tunable wavelength and 100 kHz linewidth. The wavelength is tuned to achieve the desired frequency offset. We use two polarization-maintaining couplers and two variable attenuators (VOA) to adjust CSR, as illustrated, having split the laser output. The IQ modulator is biased at the null point to generate a SSB carrier-suppressed OFDM signal. The total optical power is constant when adjusting CSR.

The SSB-OFDM signal is coupled into the fabricated chip via grating couplers. Amplification stages are used at input and output to overcome coupling losses in the unpackaged chip. The EDFAs (erbium doped fiber amplifiers) are followed by a tunable optical band pass filter (OBPF) with 0.4 nm pass-band to remove amplified spontaneous emission before PD.

On-chip, we split the optical signal into two paths via a Y branch. The signal in one path is transmitted unchanged, and then directly detected with an off-chip photodetector (PD). In the second branch, carrier suppression is realized by a two-bus MRR with a single deep notch. As the SiP components are sensitive to polarization, a polarization controller (PC) is used before the light is coupled into chip. The electrical signal after PD is captured by a real-time oscilloscope (RTO) with an 80 GS/s sampling rate, and then processed off-line with MATLAB. We reduce the sampling rate to two samples per symbol to mimic a realistic system. All processing is done at two samples per symbol.

Due to the lack of identical PDs, a single PD is time-multiplexed to convert the two chip outputs to the electrical domain in a round robin fashion. This leads to sub-optimal performance as the noise when using time-multiplexing is uncorrelated, while noise detected simultaneously on two identical PDs would cancel out. Therefore our results are somewhat pessimistic vis-à-vis the simulated identical PDs illustrated in Fig. 2.4.

2.7.3 SSBI cancellation

To visualize the efficiency of the SSBI cancellation procedure, we calculated the power spectral density of the signals in each branch, the through path and the carrier-suppressed path. For frequency offset of 12 GHz and CSR of 0 dB, Fig. 2.10a shows the signal corrupted by SSBI

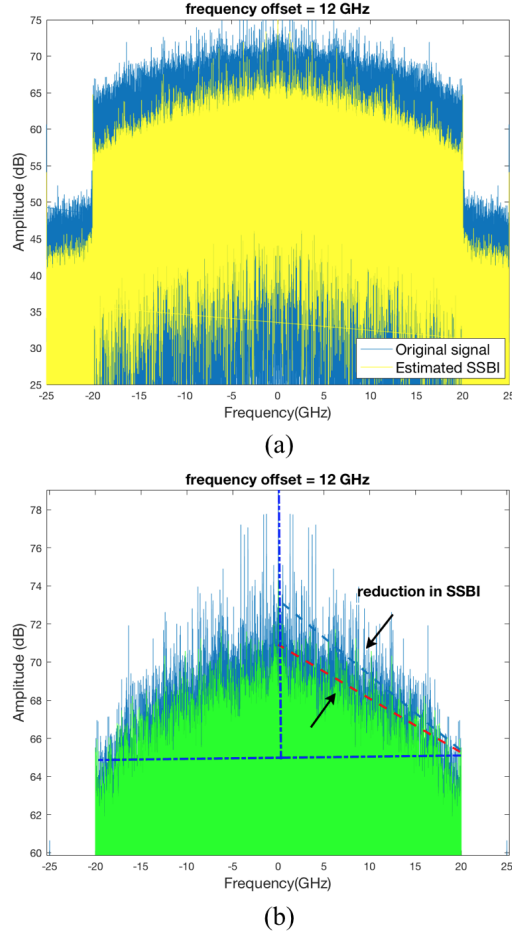


Figure 2.10: Electrical spectrum of a) signal plus SSBI noise (blue/dark) and isolated SSBI (yellow/light colored), and b) signal plus SSBI noise (blue/dark) and signal with suppressed SSBI (green/light colored)

noise (blue spectrum) and the estimated SSBI (yellow spectrum). Both spectra exhibit a triangular shape, as expected. The estimated SSBI has a lower intensity because the total power is diminished by filtering the carrier.

Fig. 2.10b recreates the signal corrupted by SSBI noise (blue spectrum), and superimposes the signal after SSBI cancellation (green spectrum). We trace two lines on each spectra to approximate the hypotenuse of the triangular spectra. Ideally we would have a flat, zero-angle spectrum. We can see that post-cancellation the spectra is flatter vis-à-vis the SSBI corrupted spectrum, with considerably reduced angle. The difference between the two spectra is an indication of the extent of SSBI reduction, the source of performance improvement.

As the residual SSBI varies across subcarriers, we expect performance per subcarrier to also vary. We transmit frames of 10^5 symbols, and estimate Q-factor using the method described in (1) and (2). For frequency offset of 12 GHz and CSR of 0 dB, i.e., the spectra in Fig. 2.10,

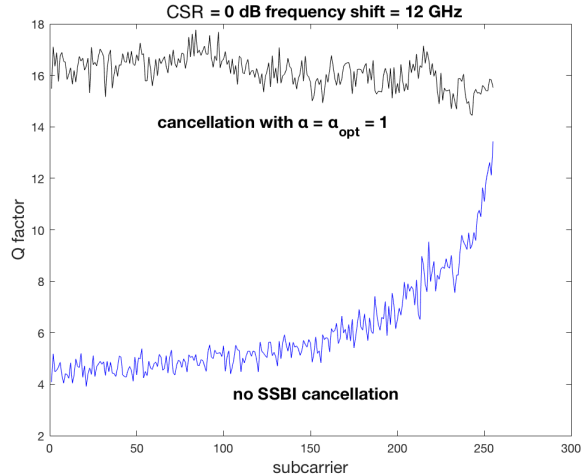


Figure 2.11: Q-factor per subcarrier

we calculate Q-factor per subcarrier and report it in Fig. 2.11. Without SSBI cancellation, we see the classic exponential Q-factor increases at higher-index subcarriers where the triangular SSBI spectrum has fallen to zero. The Q-factor is 4 dB for lowest-index subcarriers and increases to 14 dB.

After SSBI cancellation, all subcarriers have similar performance, as shown by the black curve in Fig. 2.11. While quite uniform, the higher-index subcarriers do see some degradation, though still improved performance compared to the case without SSBI cancellation. The suppression filter is most effective around the carrier frequency, i.e., in the region of lower-index subcarriers. Note that the optimal α factor (as defined in section III.C) is one. Due to the presence of an EDFA at the chip output, there is a power equalizing effect. A system with on-chip photodetection might see a different optimal α .

2.7.4 SSBI cancellation performance

We sweep the carrier wavelength to study the performance of SSBI cancellation at different frequency offsets. We also examine three levels of CSR (0 dB, 3 dB and 5 dB) to assess SSBI cancellation performance for different SSBI strength.

Fig. 2.12 shows the experimental results for average (over subcarriers) Q-factor gain in dB versus frequency offset. For each point, we sweep α and report gain for the optimal α for that data point. We see the same behavior identified in simulations in Fig. 2.7. Negative frequency offsets see little gain. Centering the notch on the carrier, zero frequency offset, is not the best strategy. As predicted in the discussion of section III.A, a positive frequency offset provides the best mitigation of non-ideal filtering.

The three curves plotted in Fig. 2.12 are for various CSR values, all yielding similar Q-factor

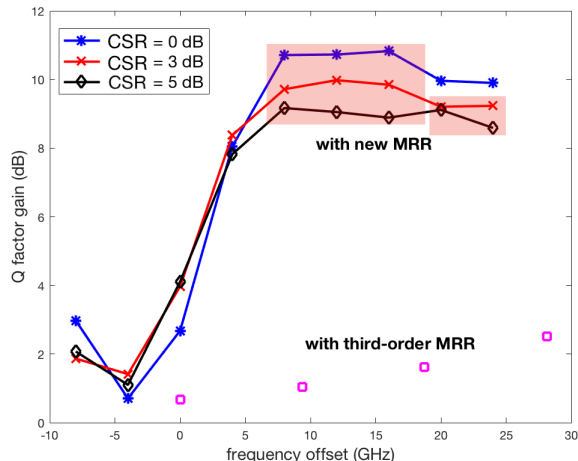


Figure 2.12: Q-factor improvement[36] in dB due to SSBI cancellation vs. frequency offset for the three values of CSR. Proof-of-concept demonstration [32] results in square markers are included for comparison.

gain. The gain is calculated with respect to Q-factor without SSBI cancellation: 4.74 dB for $CSR = 0$ dB, 6.12 dB for $CSR = 3$ dB, and 7.01 dB for $CSR = 5$ dB. The simulation results in section III predict the frequency offset to achieve best cancellation performance shifts as the CSR changes. Larger CSR leads to better performance after cancellation than small CSR values because a signal with larger carrier suffers less from SSBI. Thus the lower CSR signal experiences higher Q-factor improvement.

For comparison, we recreate in Fig. 2.12 in square markers the previously reported [32] Q-factor improvement. That demonstration used a cascaded third-order MRR with a broadened frequency response, with smaller extinction ratio and larger FWHM bandwidth. Clearly the extinction ratio and roll-over has a strong impact on SSBI cancellation.

For all three CSRs from 8-18 GHz offsets we see a uniform, high level of Q-factor gain. As MRRs are subject to temperature-induced frequency drift, this provides for more robust performance. Good levels of performance are obtained for all CSR levels for a range of 12 GHz. The Q-factor after SSBI cancellation varies from 14.7 dB to 16.2 dB for offsets in between 8 GHz and 20 GHz, over the range of CSRs.

2.8 Discussion

The experimental results shown in Fig. 2.11 and Fig. 2.12 confirm simulation predictions, and exhibit good performance after SSBI cancellation. Without SSBI cancellation, the Q-factor for all three CSRs is below 8.5 dB. The 7% forward error correction (FEC) threshold of 3.8×10^{-3} is not achievable at that Q-factor, even for QPSK modulation. We would need to use significant guard band to avoid SSBI at these CSR levels.

After cancellation, we can see significant Q-factor gain. As shown in Fig. 2.12, even with no guard band, we have a margin of 7.5 dB above the FEC threshold for QPSK over a large frequency offset range. The shaded part in Fig. 2.12 are points with Q-factor larger than 15.19 dB, where 16 QAM is possible considering the 7% FEC. With zero guard band and low CSR, the optical suppression could achieve 64 Gbits/s over a 16 GHz bandwidth. The uniform performance of different subcarriers after our optical SSBI cancellation indicates that the SSBI is well cancelled.

Our performance should be compared to that of solutions offered by other researchers [37; 38; 39; 40; 41]. Traditional approaches include a strong carrier or a guard band to avoid SSBI. More recent DSP solutions include iterative cancellation and KK. To compare our solutions with these alternatives, we fix target data rate and OSNR and assume ideal probabilistic shaping and use theoretical calculations as in [38; 39; 40; 41]. For a single polarization, single side band, direct detection system, from Shannon’s formula the required bandwidth B for the analog to digital converter (ADC) is related to the data rate R by

$$R = \eta B \log_2 \left(\frac{OSNR}{1 + CSR} \frac{B_{ref}}{B} \right) \quad (2.3)$$

where η is the spectral efficiency and B_{ref} is the reference bandwidth. We fix all other values and solve for B . We target a bit rate of $R = 200$ Gbits/s, assume a received OSNR of 30 dB, η of 0.5 for a guard band approach and 1 for other schemes, and $B_{ref} = 12.5$ GHz. In some architectures, a 3 dB penalty is imposed on the received OSNR.

For all SSBI suppression or mitigation methods, there will always be residual SSBI. To compare these techniques fairly, we assume the SSBI problem is completely suppressed with sufficient CSR (that varies by suppression techniques). Table. 2.1 shows the CSR requirements (found experimentally in cited references) and ADC bandwidth requirements B calculated from (2.3).

Strategy against SSBI	Minimum CSR (dB)	Number of PDs	Number of ADCs	Minimum ADC bandwidth (GHz)
Strong carrier [38]	15	1	1	78GHz
Guard band [39]	0	1	1	50.2GHz
Iterative SSBI cancellation [37]	9	1	1	38.3GHz
Kramer-Kronig receiver [40]	6	1	1	31.6GHz
Enhanced KK receiver [41]	3	2	2	33.4GHz
Hardware SSBI cancellation	0	2	1	29.7GHz

Table 2.1: Comparison of CSR and ADC requirements for different DD-SSB schemes with 30 dB received OSNR and 200 Gbits/s net data rate

When relying solely on a strong carrier power to make SSBI negligible, the required CSR is 15 dB [38]. As a result, we need 78 GHz optical spectrum to achieve 200 Gbits/s, an ADC to

cover the spectrum, and one PD. If we use a large guard band to avoid the SSBI, the spectral efficiency is halved, but the CSR can be as low as 0 dB[39]. Invoking the formula, the ADC bandwidth requirement is 50.2 GHz to cover the guard band of 25.1 GHz. DSP methods including iterative SSBI cancellation and KK detection could reduce the CSR to 9 dB and 6 dB respectively[37; 40; 41], leading to reduced ADC bandwidth requirements of 38.3 GHz and 31.6 GHz, respectively. With an enhanced KK receiver, smaller CSR is required compared to traditional KK, however the received signal is split at reception, invoking a 3 dB OSNR penalty. The net effect is to increase the bandwidth requirement to 33.4 GHz. For our optical cancellation solution, as verified with our experiment, the CSR could be reduced to 0 dB. Again, a 3 dB OSNR penalty is included given the y-branch splitting. The calculated ADC bandwidth requirement for optical SSBI cancellation is 29.7 GHz.

PONs are severely constrained in cost. For instance, single feeder PONs allow the uplink to be borne by the carrier distributed on the downlink. Low required CSR means the limited carrier power can provide better performance on both the downlink and uplink. Components must also be cost and power efficient in a PON. Higher bandwidth ADCs will significantly increase the deployment cost. Our solution provides the best solution vis-à-vis low CSR, bandwidth efficiency and required ADC bandwidth.

Even while incurring a 3 dB loss in OSNR at the receiver front end in our solution, the lower CSR requirement results in performance improvement. Among all direct detected SSB schemes, optical cancellation has the potential to realize the lowest required CSR, as well as avoiding a large guard band. The only drawback is the use of two PDs to achieve balanced detection. The SiP solution and integrated PD means this additional complexity should only incur modest cost. Balanced detection offers the additional advantage of suppressing common mode noise.

Due to the polarization sensitivity of SiP components, we used polarization control in our demonstrations. In future designs, on-chip polarization splitter rotators would be included to achieve polarization diversity and obviate polarization control. For temperature stability, an additional on-chip PD and slow electronic feedback would be needed. Our MRR design provides a level of robustness against temperature induced frequency drifting, thus the feedback loop requirements would not be demanding.

2.9 Conclusion

We have fabricated and experimentally examined a SiP SSBI cancellation subsystem for DD-OFDM. System simulations confirmed the effectiveness of SiP SSBI cancellation and predicts the influence of frequency offset on SSBI cancellation. Experiments with the fabricated chip validates simulation results. We demonstrate significant Q-factor gain. The Q-factor can be increased to 15.57 dB, 16.09 dB and 16.19 dB, respectively, for CSR = 0 dB, 3 dB, 5 dB. The

spectral efficiency is high, as no guard band is used. Lower CSR is required compared to both standard and enhanced KK, and no extensive DSP is needed as compared to the enhanced KK method. The SIP system offers low complexity and cost. Our subsystem is proved to be robust across a wide range of frequency offset via experiment.

Chapter 3

Optimizing SiP Microring Resonators to Suppress Interference in OFDM Detection

3.1 Résumé

Nous exécutons l'analyse systématique du schéma d'annulation SSBI précédemment proposé. Le schéma activé par la photoniques au silicium fournit une solution intégrée basée sur le résonateur à micro-anneau, qui est relativement vulnérable aux changements de température. Nous introduisons le facteur-Q minimum garanti, soit une nouvelle métrique de performance, pour évaluer la robustesse d'annulation SSBI contre la dérive de fréquence induite par les changements de température. Avec le paramètre nouvellement introduit, nous maximisons l'efficacité spectrale sous différentes conditions du système en optimisant les paramètres de conception contrôlables. Finalement, les résultats de la simulation du système fournissent des indications sur la conception du résonateur à micro-anneau ainsi que la valeur de la bande de garde et le choix du format de la modulation pour obtenir la plus grande efficacité spectrale.

3.2 Abstract

We run the systematic analysis on the previously proposed SSBI cancellation scheme. The silicon photonics enabled scheme provides an integrated solution based on microring resonator, which is relatively vulnerable to temperature changes. We introduce a new performance metric, minimum guaranteed Q-factor to evaluate the SSBI cancellation robustness against the frequency drift induced by temperature changes. With the newly introduced parameter, we maximize the spectral efficiency under different system conditions by optimizing controllable design parameters. Finally the system simulation results provide a guidance on the microring resonator design as well as the guard band value and modulation format choice to achieve the

highest spectral efficiency.

3.3 Context and Contributions

This thesis covers the use of SiP subsystems for OFDM with direct detection, as well as SiP for 5G radio over fiber. In this chapter we continue to look at SSBI suppression for OFDM, while 5G radio over fiber is covered elsewhere.

The major contribution in this chapter is the enhancement of previously proposed SSBI cancellation system. Polarization diversity is included in the system to overcome the sensitivity of polarization for SiP PICs. And scaling factor is realized on-chip instead of applying digitally to further decrease the receiver complexity.

Another drawback of SiP photonic integrated circuits (PICs) is the temperature dependency. To evaluate the SSBI cancellation performance under unstable frequency offsets, we proposed a new metric, minimum guaranteed Q factor to model the temperature effects.

Based on the new metric, we run extensive simulations to explore the trade-offs between system design and operation. A generic guidance on the MRR designs and system operation parameters is provided to optimize the performance in practical applications.

3.4 Introduction

The global communications infrastructure has proven critical to economic development and well-being, especially in times of crisis. With distance learning and working entering the mainstream we must increase capacity and transmission rates in access networks [42]. In particular, the workhorse passive optical networks (PONs) are moving towards higher nominal line rates, 25G or 50G[43; 44; 45]. Many challenges exist for next generation PON, with standardization yet to be finalized. Of particular concern is the limited power budget, particularly for upstream data.

While coherent detection may be introduced at the optical line termination (OLT) [46], this solution is unacceptable for cost-sensitive optical network units ONUs at customer premises. As ONUs will continue to use low cost direct detection, the carrier-to-signal ratio (CSR) must be high to suppress signal to signal beating interference (SSBI). To increase the uplink power budget for uplink, some carrier power could be reallocated from download detection - provided another means of SSBI suppression is available [47]. Several solutions for SSBI have been studied using digital signal processing (DSP), e.g., the Kramer Kronig (KK) detector[21] could reduce the CSR requirement to 6 dB. Hardware solution can further reduce the required CSR (and also reduce DSP complexity and power consumption), however cost is increased by extra components, such as couplers, filters and detectors. However, silicon photonics (SiP)

could tip the balance toward hardware solutions [9]. Additional components on SiP chip have little impact on overall cost due to integration. Note that SSBI is impacted by both CSR and guard band, so both can be optimized and traded off to improve the uplink power budget.

In previous work [48], we experimentally examined SSBI cancellation scheme in SiP. Good performance was observed with only 0 dB CSR and a zero guard band OFDM signal. We used a fabricated microring resonator (MRR) filter in our ONU receiver. The MRR had $\kappa = 0.25$ and we controlled the resonance frequency. In deployed systems, the MRR frequency cannot be stabilized perfectly, especially at reasonable cost. Therefore, the residual, uncompensated frequency drift will effect performance. The MRR can be designed to be robust to that delay.

In this paper, we attack the design of MRR-based subsystems for SSBI suppression in the presence of residual frequency drift. We define a performance metric for an MRR subject to residual drift across a frequency span: the minimum guaranteed Q-factor. This metric varies with the CSR and guard band operating points. We explore MRR design sensitivity to frequency instability. We use our simulation results to trade-off between performance and robustness. These results provide a MRR filter design guide for SSBI suppression. We predict performance of various possible designs and operation points to illustrate the utility of our performance metric. In particular we find the MRR design that maximized spectral efficiency for a given span of frequency drift.

3.5 SSBI cancellation using MRR

Figure 3.1a shows the SSBI cancellation scheme in SiP from [48]. The microring performs the carrier rejection, thus creating an output with the pure SSBI at the photodetector (PD). By balanced detection, we subtract the SSBI from the signal detected in the upper arm. Most SiP structures are sensitive to polarization, resulting in polarization dependent loss or loss of signal. Figure 3.1b is a polarization divers solution to the shaded section in Fig. 3.1a. A polarization splitter rotator (PSR) converts light with arbitrary polarization state into pure TE modes across two outputs (ratio of power depending on incident polarization). In [48] performance of SSBI rejection was improved by introducing a scaling factor between the two photodetected powers. The phase shift and 2×2 coupler is a means of tuning to any scaling factor. The phase shift is adjusted to alter the splitting ratio between two output arms.

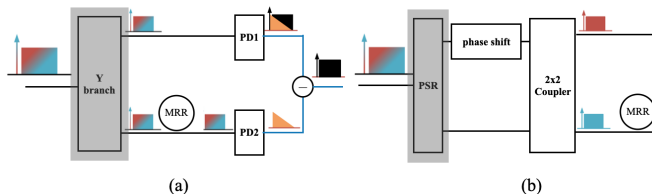


Figure 3.1: SSBI cancellation subsystem a) as examined experimentally in [48], and b) altered to achieve polarization diversity and tunable scaling factor.

Due to non-ideal filtering, we must trade-off the unwanted filtering of the signal and the

residual carrier. A residual carrier in SSBI isolation results in a signal-to-noise ratio (SNR) penalty, while the unwanted filtering of the signal band causes incomplete SSBI subtraction. Both the scaling factor α between PD powers and an MRR frequency offset can implement the trade-off.

The optimal frequency offset and scaling factor in [48] applied to one specific ring design and fixed guard band value. In this paper we discuss the system optimization more generally. Three dimensions are considered: ring design, operating point (CSR and guard band), and frequency drift. We simulate the system performance for all these parameters to give a global view. The simulation results could be used to guide the use of SSBI cancellation - from MRR design to operation point choice to achievable spectral efficiency.

3.5.1 Ring Design

The SSBI cancellation performance is determined by the reconstruction of pure SSBI, which requires precise and sufficient carrier rejection. The carrier suppression is realized by a single in-line microring resonator. As free space range is not critical for the SSBI cancellation, we could use a relatively larger ring (radius around $45 \mu m$). The coupling coefficient κ determines the quality factor and extinction ratio. The frequency response of rings with increasing κ value were simulated in the Lumerical Interconnect and are presented in Fig. 3.2. A larger coupling coefficient results in larger extinction ratio and thus better carrier suppression. Consider the filter quality factor, wavelength over full width half maximum bandwidth. This factor drops from 6036 to 2950 as κ increases from 0.1 to 0.4. A lower factor indicates poorer SSBI reconstruction and incomplete SSBI cancellation. In our simulations, κ is swept from 0.1 to 0.5 to predict the performance variations.

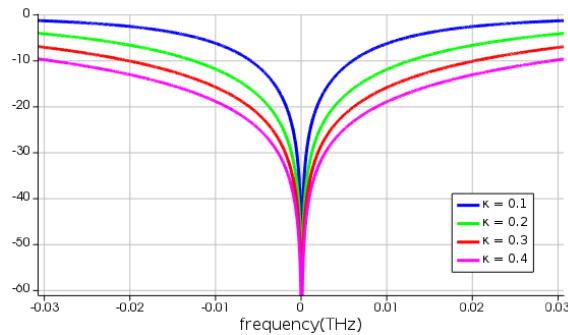


Figure 3.2: MRR frequency response in the through port for various κ parameters

Instead of subtracting the reconstructed SSBI directly from the detected signal, a scaling factor α is optimized to balance the incomplete SSBI cancellation and detected signal power penalty. For the similar consideration, we could tune the MRR resonance peak slightly away from the carrier to balance the two opposite effects. In this paper, we always sweep the scaling factor to optimize performance. The frequency offset of the MRR, however, is optimized for specific levels of residual frequency drift. While an unambiguous optimal offset exists for zero drift, variability in performance due to drift from the target offset must be studied more carefully.

3.5.2 Performance Metrics

We simulate the SSBI cancellation scheme based on a direct-detected OFDM system with 16 GHz bandwidth and guard band we sweep from 0 GHz to 16 GHz. The maximum guard bandwidth examined yields SSBI that is negligible. The modulation format is QPSK and the OSNR is 25 dB. We use the bit error rate (BER) averaged over each subcarrier as the performance metric. That is, the Q-factor is calculated from the average BER for QPSK per

$$Q = \sqrt{2} \cdot \operatorname{erfcinv}(2 \cdot \text{BER}) \tag{3.1}$$

and should not be confused with the filter quality factor discussed earlier. We use the estimated Q-factor to determine the highest order modulation achievable, using Q-factor thresholds at 10^{-3} BER for each modulation order. Different CSRs, from 0 dB to 9 dB, are simulated.

Having set the system parameters, there remains one important issue for SiP applications. The temperature change will change the effective index of the material and change the MRR response. Even with one Celsius degree change, 10 GHz frequency offset of MRR occurs. We could use a thermo-electric cooler or a feedback loop to control the temperature of SiP chips. But practical constraints on cost and complexity lead to some residual temperature effects. We propose a performance metric, the minimum guaranteed Q-factor, to evaluate the system performance in the presence of some frequency instability

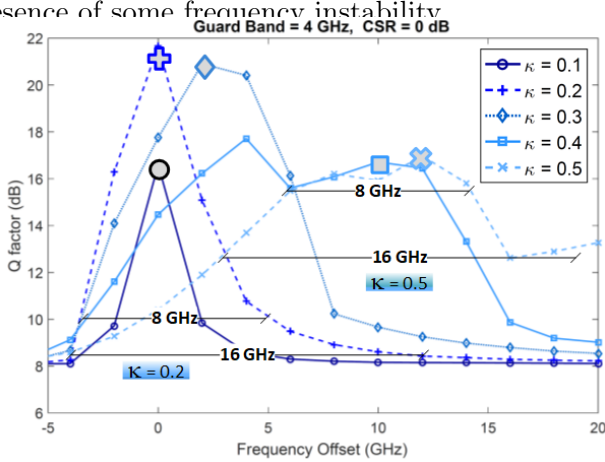


Figure 3.3: Q-factor vs. frequency offset for various κ ; illustrations of two sets of 8 and 16 GHz spans and the guaranteed minimum Q within that span (one set for $\kappa = 0.2$ and one set for $\kappa = 0.5$).

Figure 3.3 shows the Q-factor vs. frequency offset after SSBI cancellation for various coupling coefficients κ . For negative frequency offset the Q-factor falls quickly. In this situation the resonance peak falls in the signal band, resulting in very poor SSBI reconstruction. For positive frequency offset the Q-factor slopes tend to be more gradual; in this region we were able to optimize the scaling factor at each data point, helping to reduce the slope. The scaling factor function could be implemented on chip as illustrated in Fig. 3.1b.

Each κ has an optimal frequency offset (see large markers in Fig.3.3). Of even greater importance is the variation with κ of the slopes leading to and away from those peaks. We define

two frequency offset spans (8 GHz and 16 GHz) that represent reasonable residual drifts when using thermal stabilization of the target offset. Instead of targeting the frequency offset giving peak Q, we propose targeting the midpoint of the span of frequency drift as the optimal frequency offset. In the case of $\kappa = 0.5$ and a 16 GHz span, this approach leads to targeting 10 GHz offset instead of zero offset.

Algorithm 1: Minimum guaranteed Q for given span

Input: Q-factor vs. frequency offset (as in Fig. 3.3), *step* of frequency offset sweep and *span*

Output: minimum guaranteed Q (Q_m) and optimal frequency offset f_0

```

1 Find all the peaks on the curve,  $P_1, P_2 \dots P_k$  ;
2 Start with  $P_1$ , record the initial span as  $[f_l, f_h]$ , where  $f_l = f_h = f_{P_1}$ . The normalized
   span  $n_s$  is calculated via  $n_s = span/step$  ;
3 for  $n = 1, n < n_s$  do
4    $Q_m = Q_{P_1}$  ;
5   if  $(f_l - step)$  exceeds boundary then
6      $f_h = f_h + step$  ;
7      $Q_m = \min(Q_m, Q_{f_h})$  ;
8   else if  $(f_h + step)$  exceeds boundary then
9      $f_l = f_l - step$ ;
10     $Q_m = \min(Q_{f_l}, Q_m)$  ;
11   else
12     if  $Q_{f_l-step} > Q_{f_h+step}$  then
13        $f_l = f_l - step$  ;
14        $Q_{temp} = Q_{f_l}$  ;
15     else
16        $f_h = f_h + step$  ;
17        $Q_{temp} = Q_{f_h}$  ;
18      $Q_m = \min(Q_{temp}, Q_m)$  ;
19    $n = n + 1$  ;
20 Repeat the same process for other peaks ;
21  $Q_m = \max(Q_{P_1}, Q_{P_2}, \dots, Q_{P_k})$   $f_0 = (f_h + f_l)/2$ 
22 final ;
23 return  $Q_m$  and  $f_0$  ;

```

We define the minimum guaranteed Q for a given frequency span using the curves of Q-factor vs. frequency offset in Fig. 3.3. By tuning the MRR to the midpoint of the frequency span for a given κ , a drift anywhere within the span will never go lower than the minimum guaranteed Q. The peak Q-factor is a special case for minimum guaranteed Q where the frequency drift is zero. When the frequency drift is non-zero, we use a greedy algorithm described in algorithm block to find the minimum guaranteed Q and use this quantity in our further analysis.

In the case of $\kappa = 0.2$ the minimum guaranteed Q is 10.2 dB and 8.4 dB for spans of 8 GHz and 16 GHz, respectively. As discussed previously, an MRR with larger κ exhibits larger

extinction ratio but poorer quality factor, yielding a more shallow shape of the notch. The precise confinement of carrier rejection is sacrificed to obtain the robustness against frequency drift. So we can find a lower peak Q-factor but a higher guaranteed Q-factor for $\kappa = 0.5$. The minimum guaranteed Q is 15.7 dB with 8 GHz drift. Even with a larger drift of 16 GHz, a 13 dB Q-factor could be maintained, which is not achievable with $\kappa < 0.3$.

3.6 Simulation Results

In simulations reported in this section, κ is swept from 0.1 to 0.5 in divisions of 0.05. The CSR is explored from a rather low 0 dB to 9 dB every 1 dB. To focus on scenarios where SSBI dominates ASE noise, we set the OSNR. The methodology we introduce could be adapted to any link and is not limited to the SSBI-limited case.

The Q-factor thresholds for QPSK, 8 QAM, 16 QAM and 32 QAM are 9.8 dB, 12.6 dB, 13.5 dB and 16.6 dB respectively. We indicate these contours in our 3D plots to indicate boundaries for passing from one modulation format to another. Direct detection limits us practically to 32 QAM.

3.6.1 Baseline performance with no drift

Figure 3.4 shows the Q-factor after SSBI cancellation for CSR of 0 dB. Both guard band (y-axis) and κ are varied. The Q-factor significantly benefits from the increased guard band, but of course then sacrifices spectral efficiency. When there is no frequency drift, MRR with smaller κ creates precise carrier suppression and thus exhibits better SSBI cancellation performance. An MRR with smaller κ requires smaller guard band compared to an MRR with larger κ for QPSK, 8 QAM, and 16 QAM.

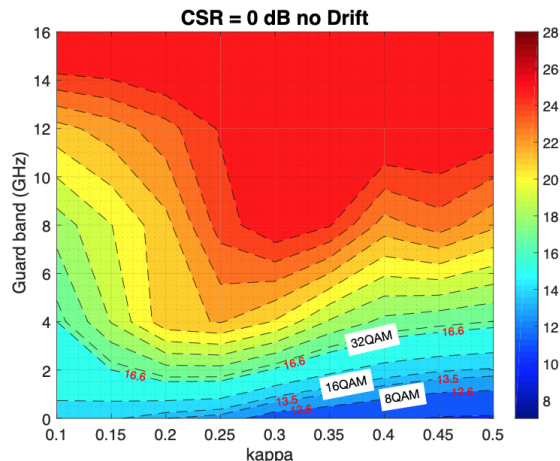


Figure 3.4: Color gives peak Q in dB (zero drift) at 0 dB CSR as a function of guard band and kappa; achievable QAM modulation for 10^{-3} BER indicated on appropriate contour and annotated with required Q.

Again assuming with no frequency drift and using the optimal offset, Q-factors after SSBI cancellation with Fig. 3.5 examines various CSR. With larger CSR, the SSBI is relatively

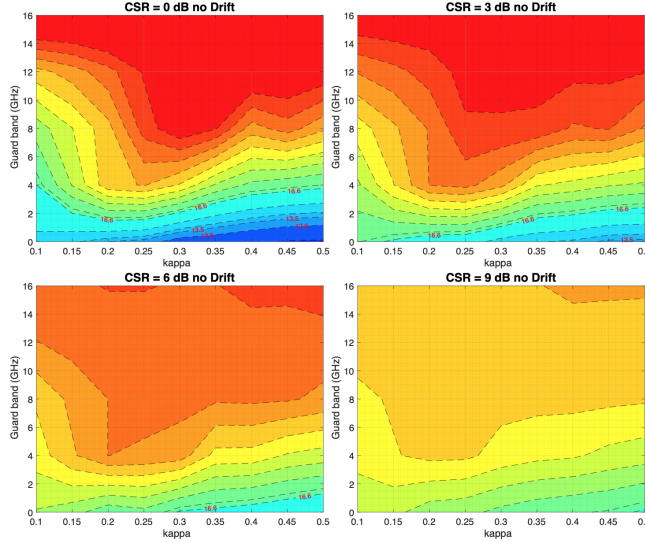


Figure 3.5: Color gives peak Q in dB (zero drift) as a function of guard band and kappa; CSR is varied per graph, and color scale as in Fig. 3.4.

weak compared to the desired beat between larger carrier and signal. That explains why larger CSRs exhibit better overall performance, and smaller required guard band and higher order modulation. However, for larger CSRs, the best achievable Q-factor at high guard band is slightly lower. The simulation is run under a normalized received power, which is shared by the carrier and signal. Higher CSR indicates weaker signal power and poorer performance against ASE noise. This explains why the performance degradation is more obvious at large guard band where the SSBI is weak and ASE noise starts to dominate the performance.

From the four sub-figures shown in Fig. 3.5, without consideration of frequency drift, the strategy for MRR κ optimization is unaffected by CSR. We always benefit from the precise carrier rejection of smaller κ .

3.6.2 Effects of residual frequency drift

We now introduce the frequency drift into our simulation. The SSBI cancellation performance with a frequency drift that may span 12 GHz is given in Fig. 3.6. In the presence of residual frequency drift, the κ optimization for the MRR exhibits a totally different trend. Comparing Fig. 3.5 and Fig. 3.6 at 0 dB CSR, we see that the deepest trough (best Q for a given guard band) is at κ equal .23 and .42, respectively. A similar shift in optimal κ is seen at other CSR values as well. To overcome the frequency drift, MRR with larger κ is favored due to its shallow response over a wide range.

We combine the guard band and supported modulation format to introduce a new metric, spectral efficiency, to evaluate the system performance. The spectral efficiency η is

$$\eta = \log_2(M) \cdot BW_s / (BW_s + BW_{gb})$$

where the M is the highest modulation format supported by the minimum guaranteed Q-

factor, and BW_s and BW_{nh} are the signal and guard band bandwidths, respectively.

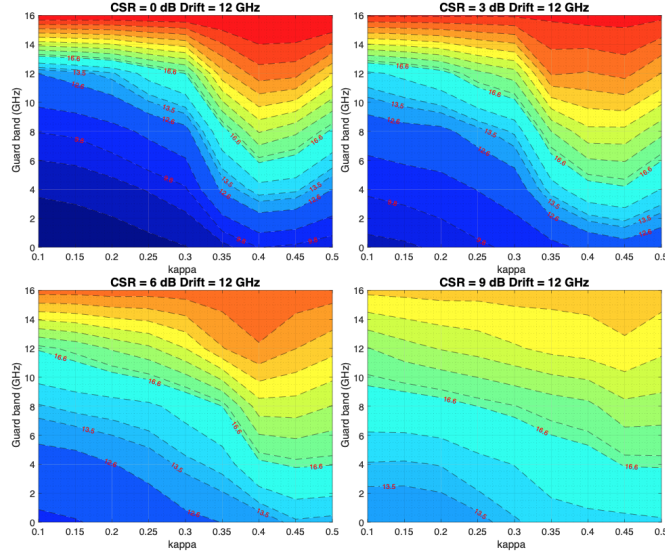


Figure 3.6: Color gives minimum guaranteed Q in dB for a drift spanning 12 GHz; color scale as in Fig. 3.4; CSR varied per graph, and color scale as in Fig. 3.4.

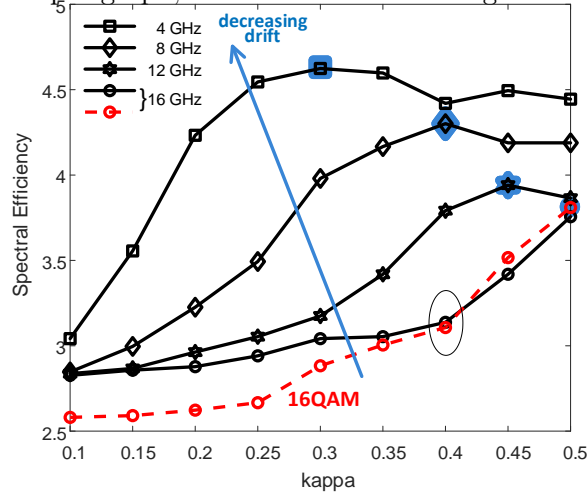


Figure 3.7: Spectral efficiency in bits/s/Hz at 25 dB OSNR, 5 dB CSR for four spans of frequency drift (4, 8, 12 and 16 GHz); 32QAM modulation unless otherwise labeled.

The guard band and Q-factor can be traded-off to optimize the spectral efficiency. We fix CSR to 5 dB and OSNR to 25 dB and present spectral efficiency in Fig. 3.7 for 32QAM modulation. A different curve is presented for each residual frequency drift span of 4, 8, 12 and 16 GHz. As the frequency drift decreases, the spectral efficiency increases, as expected. The maximal spectral efficiency at each drift is indicated by an enlarged blue marker in Fig. 3.7. Following the trends we see in Fig. 3.6, the optimal κ moves to left (decreases) as the frequency drift decreases.

Even with relatively large frequency drift (12 GHz) 32 QAM provides highest spectral efficiency, indicating that only a small guard band is required. The system performance is not strongly limited by the SSBI. In most cases, 32QAM provides the highest spectral efficiency, but not always. In in Fig. 3.7 we also plot spectral efficiency for 16QAM in the case of high-

est drift examined. The spectral efficiency curves for the two modulation formats intersect (see oval), meaning that at larger κ a smaller guard band is the source of increased spectral efficiency.





Span	CSR = carrier-to-signal ratio									
	0 dB	1 dB	2 dB	3 dB	4 dB	5 dB	6 dB	7 dB	8 dB	9 dB
4 GHz										
best kappa	0.35	0.35	0.3	0.3	0.35	0.3	0.35	0.35	0.3	0.3-0.4
best offset (GHz)	6.0	6.0	4.0	4.0	4.0	4.0	4.0	4.0	4.0	4.0
modulation	32QAM	32QAM	32QAM	32QAM	32QAM	32QAM	32QAM	32QAM	32QAM	32QAM
guard band (GHz)	3.19	2.75	2.48	2.10	1.65	1.36	1.00	0.72	0.41	0.00
8 GHz										
best kappa	0.35	0.35	0.35	0.35	0.35	0.4	0.4	0.4	0.45	0.45
best offset (GHz)	4.0	5.0	5.0	4.0	4.0	6.0	6.0	5.0	4.0	6.0
modulation	32QAM	32QAM	32QAM	32QAM	32QAM	32QAM	32QAM	32QAM	32QAM	32QAM
guard band (GHz)	4.26	3.72	3.23	2.90	2.95	2.58	2.25	2.24	2.10	1.85
12 GHz										
best kappa	0.4	0.4	0.4	0.45	0.45	0.45	0.45	0.5	0.5	0.5
best offset (GHz)	5.0	5.0	6.0	8.0	10.0	8.0	6.0	8.0	8.0	6.0
modulation	32QAM	32QAM	32QAM	32QAM	32QAM	32QAM	32QAM	32QAM	32QAM	32QAM
guard band (GHz)	5.90	5.20	4.57	4.22	3.87	4.27	3.77	3.45	3.35	3.75
16 GHz										
best kappa	0.45	0.45	0.45	0.45	0.5	0.5	0.5	0.5	0.4-0.5	0.4-0.5
best offset (GHz)	8.0	6.0	6.0	7.0	8.0	12.0	12.0	10.0	6.0-9.0	5.0-8.0
modulation	32QAM	32QAM	32QAM	32QAM	32QAM	16QAM	16QAM	16QAM	16QAM	16QAM
guard band (GHz)	7.43	7.37	6.72	6.08	5.42	0.80	0.00	0.00	0.00	0.00

Table 3.1: MRR design guide at 25 db OSNR for optimizing SSBI cancellation; best kappa and offset are the κ and MRR frequency offset setting yielding highest spectral efficiency. We produced curves such as those in Fig. 3.7 for each CSR from 0 to 9 dB. We retain the parameters for optimal spectral efficiency: the modulation format, the guard band, MRR κ and frequency offset setting. The results are tabulated in Table. 3.1, including the achievable spectral efficiency. The points highlighted in Fig. 3.7 are indicated by markers in Table. 3.1.

As expected, we see in Table. 3.1 that smaller guard band is required with larger CSR and smaller frequency drift. Also, higher order modulation format is preferred in most cases. Our methodology provides both the best frequency offset to take into account the drift (see Figure. 3.3), and the best kappa to maximize spectral efficiency (see Fig. 3.7). The design guide in Table. 3.1 assures the SSBI cancellation is exploited to the best degree possible.

3.7 Conclusion

We have performed a comprehensive simulation of the SSBI cancellation subsystem in SiP. The frequency instability of the MRR has been addressed in a design approach that adjusts the subsystem (MRR resonant frequency, operation of the MRR at a frequency offset, scaling factor in the subsystem) to achieve maximal spectral efficiency. To achieve the design process, we introduced a new evaluation metric, the minimum guaranteed Q-factor, that quantifies the effect of frequency drift. Our methodology can capture the trade off of guard band, CSR and modulation format to find the sweet spot where system effective bit rate can be optimized. Our simulation technique could guide the MRR ring design and system operations to achieve the best performance while meeting real engineering challenges.

Chapter 4

Silicon Photonic Subsystem for Broadband and RoF Detection While Enabling Carrier Reuse

4.1 Résumé

Nous validons expérimentalement un sous-système photonique au silicium conçu pour les réseaux optiques passifs avec la réutilisation de porteuses. Le sous-système est destiné aux futurs PONs multiplexés par répartition en longueur d'onde (WDM). Il permet aux signaux radio-sur-fibre de cohabiter dans une tranche de longueur d'onde assignée sans perturber le signal PON et en conservant la puissance de la porteuse pour la liaison montante. Un modulateur à micro-anneau remodule la porteuse résiduelle pour la liaison montante RoF. Nous avons détecté avec succès la chute d'un signal à large bande de 8 GHz et de cinq signaux radio-sur-fibre de 125 MHz. Deux signaux radio-sur-fibre de 125 MHz sont remodulés sur la porteuse. Le signal de liaison montante présente de bonnes performances, ce qui valide que les signaux de liaison descendante résiduels ont été bien rejetés par les filtres à micro-anneau. Le sous-système conserve une porteuse propre pour la remodulation avec un bon ratio signal/porteuse.

4.2 Abstract

We experimentally validate a silicon photonic subsystem designed for passive optical networks with carrier reuse. The subsystem is intended for future wavelength division multiplexed (WDM) PONs. It enables radio-over-fiber signals to cohabit an assigned wavelength slot without perturbing the PON signal, and conserving carrier power for the uplink. A microring modulator remodulates the residual carrier for the RoF uplink.

We successfully detected the dropped an 8 GHz broadband signal and five 125 MHz radio-over-fiber signals. Two 125 MHz radio over fiber signals are remodulated onto the carrier. The uplink signal shows good performance, validating the residual downlink signals have been well rejected by the microring filters. The subsystem conserves a clean carrier for remodulation with good signal-to-carrier ratio.

4.3 Context and Contributions

This thesis covers the use of SiP subsystems for OFDM with direct detection, as well as SiP for 5G radio over fiber. In the previous chapters we look at SSBI suppression for OFDM, while 5G radio over fiber is discussed in this chapter.

The major contribution in this chapter is the experimental demonstration of a SiP subsystem for PON with carrier reuse and 5G RoF compatibility. The subsystem enables the simultaneous detection of RoF signals and PON signal over the same assigned wavelength slot.

Ensuring the sufficient performance of RoF and PON signal detection, minimum carrier power are leached off for each detection. Effective downlink signal suppression is realized to leave a clean and strong carrier for remodulation. Then we generate the RoF uplink signal via a MRM.

We successfully detected an 8 GHz broadband signal and five 125 MHz radio-over-fiber signals simultaneously. And two 125 MHz radio over fiber signals are remodulated onto the same carrier. The generated uplink RoF signal is 13 dB over the downlink signals, indicating their robustness against the crosstalk from residual downlink signals.

4.4 Introduction

The rapid growth of mobile services and video streaming is driving requirements for greater bandwidth and higher quality communication services. Passive optical networks (PONs) provide low loss fiber transmission and silicon photonics can bring down the cost of transceiver technologies. Additional PON revenue streams can be created by supporting heterogeneous signals - both basic broadband network access and radio over fiber (RoF) signalling for 5G femtocells [49; 50]. Expanded services must conserve features keeping costs low for PONs: colorless operation with carrier reuse and a single fiber structure (as opposed to a dual feeder) [51; 52; 53].

Silicon photonics can realize highly integrated, low cost and small footprint systems, attributes particularly attractive in the cost sensitive PON market [54; 55]. Though several companies already provide single-chip silicon photonics integrated circuits (PICs) that include all transmit and receive functions, those solutions typically employ coherent detection and incorporate co-

packaged laser sources. A PON solution should avoid lasers to lower cost and maintain colorless transceivers.

We propose an integrated transceiver solution for PON with carrier reuse. The demonstrated ONU subsystem is designed for the optical line terminal (OLT) supporting 1) the hybrid direct detection of broadband signals and RoF signals within the same wavelength slot, as well as 2) the remodulation of the carrier for the uplink signal. Cascaded microring resonators (MRRs) assure the isolation of received RoF and broadband signals from one another; they also work as routing components, further decreasing system complexity. Separate on-chip photodetectors (PDs) provide the simultaneous detection of RoF and broadband signals. The MRRs leach off the minimum carrier power needed for each detection, and suppress downlink signals to leave the residual carrier free for remodulation via an on-chip microring modulator (MRM). In our experiment we do a proof of concept with RoF signals of various widths and placement to examine the feasibility of SiP resonant structures for this application. To support the RoF signals, we create a SSB OFDM signal with guard band, where the RoF signals are transmitted.

Direct detected single sideband OFDM (DD-SSB OFDM) with carrier reuse is a promising solution for next generation PONs. It is particularly flexible in sculpting both time and frequency resources [56], and uses low cost direct detection. To avoid fading induced by chromatic dispersion [24], single side-band OFDM is employed. Our demonstrations assume DD-SSB OFDM, but are equally valid for other broadband modulation formats.

The paper is organized as follows. We first discuss the details of the fabricated OLT subsystem in section 1. In section 2 we explain the experimental setup in detail. In section 3 we focus on the hybrid detection section of the OLT subsystem. After discussing the design and characterization of the two sets of cascaded MRRs, we examine the downlink performance of RoF and OFDM experimentally. In section 4 we first explain the design and characterization of the MRM to be used for RoF uplink via remodulation of the downlink carrier. The performance of the MRM modulated RoF uplink is evaluated experimentally, with and without the downlink detection in place. Finally, some concluding remarks are made.

4.5 Subsystem Design

The subsystem architecture and operating principle are illustrated in Fig. 4.1. The upper section shows the PIC with two stages of cascaded pairs of MRRs and a final stage of an MRM. The notations (A), (B) and (C) located near MRR set1, MRR set2 and the MRM, respectively, indicate reference probe points for input spectra. The lower section shows a cartoon of the optical spectrum as signals propagate through the subsystem. The input spectrum has a red block to represent the OFDM (basic broadband network access) signal; the black arrow is the optical carrier. The guard band between the carrier and OFDM signal contains a narrowband

RoF signal represented by a narrow black block. As the guard band is as wide as the OFDM signal, signal to signal beating interference (SSBI) can be eliminated in the electrical domain by a bandpass filter over the OFDM signal.

Consider the spectrum marked (A) in the lower section of Fig. 4.1. The first pair of cascaded MRRs (MRR set1 drawn as orange ovals, with its drop port passband sketched in orange dotted lines below) will drop the RoF signal. The MRR is tuned to cut only enough carrier power for RoF detection. The through path sees the RoF signal suppressed.

Consider next the spectrum marked (B) in the lower section of Fig. 4.1. The signal with suppressed RoF enters the second pair of cascaded MRRs (MRR set2 drawn as green ovals, with its drop port pass band sketched in green dotted lines below). The second cascade drops the OFDM signal, again cutting just enough of the optical carrier for direct detection. Both cascaded MRRs are thermally tuned via metal deposits to adjust their resonance peak distance, extinction ratio and central wavelength. The two MRR sets are tuned individually.

Referring finally to the spectrum marked (C) in the lower section of Fig. 4.1, the final stage remodulates the carrier with uplink RoF signals. The blue blocks to either side of the carrier and superimposed on the residual RoF downlink represent the output of the MRM.

The RoF signals are dropped firstly to an on-chip PD. The OFDM signal and most carrier power pass through the first MRR set. We tune these MRRs to confine their response to cover the narrowband RoF signals, avoiding undesired filtering of the carrier and OFDM signal. Only a very low level of the OFDM signal is dropped at the first MRM set, avoiding SSBI

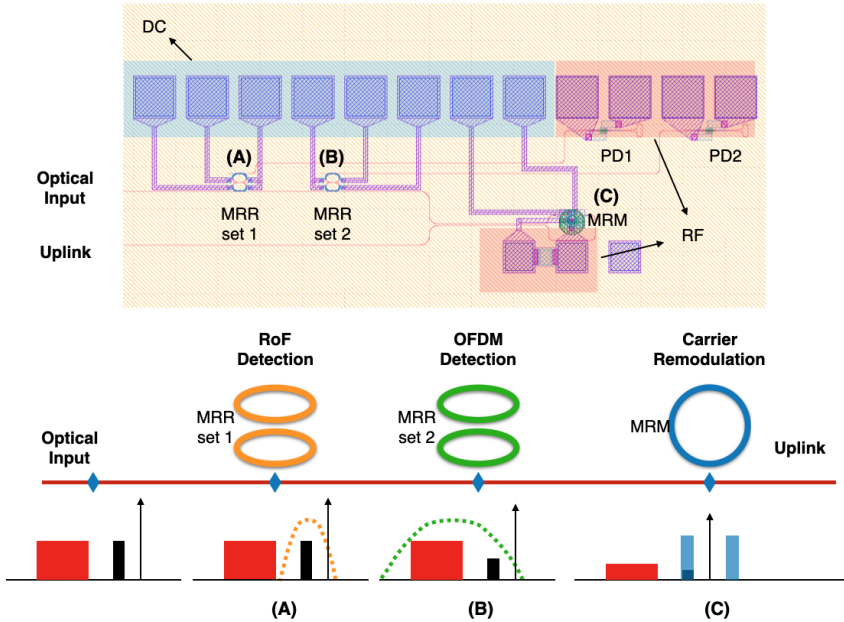


Figure 4.1: Principle of operation of the SiP subsystem. MRR drop ports are not shown.

induced degradation of RoF detection.

The second MRR set sees the residual downlink RoF signal and lightly attenuated downlink OFDM signal and carrier. As shown in spectrum (B), we drop the OFDM signal and a part of the carrier to a second on-chip PD. A more shallow response is required from these MRRs to cover the wideband OFDM signal. The large guard band ensures SSBI is out-of-band for OFDM detection. In the absence of SSBI, we can reserve most carrier power for the uplink.

The final sketch of the spectrum (C) shows our strategy of suppression of the downlink signals by the MRR stages, and uplink RoF generation. The uplink can exploit spectrum on either side of the carrier if needed. An IQ modulator could be used to generate a single sided RoF signal if preferred. Note that the RoF signals are represented as a single block, but may have multiple narrowband signals (for multiple antennas, for instance) within that pass-band.

While our experiment shows the uplink exiting a separate port, in future designs the remodulated signal could be guided through another optical path for a true single feeder structure. For instance, a reflective structure could be added to the MRM output to send the uplink signal back along the same path. The MRR filtering would then allow single sideband modulation without an IQ MRM. The MRM double sided uplink signal would see the left sideband filtered by the cascaded MRR sets, while the right sideband would remain (mostly) unchanged. As the dropped left sideband of the uplink signal would be guided to a different MRR port than the one connected to the PDs, the downlink detection would not be perturbed.

Since silicon photonics is based on high-index-contrast waveguides compatible with CMOS technology, high speed optical modulators [57] could be realized along side the common passive components. Figure 4.1 shows the transceiver subsystem layout we sent for fabrication. The ultra small footprint and low power consumption (down to Fj/bit), of the MRM lowers overall cost. The total footprint of our proof-of-concept subsystem is $0.5 \text{ mm} \times 1.475 \text{ mm}$, dominated by the bond pads for DC and RF probes. The blue shaded pads are for DC connections for thermal tuning. The red shaded pads are for RF probes to 1) capture the detected downlink signal and 2) carry the RF uplink signal for remodulation of the carrier. The ability to tune the wavelengths of the MRRs and MRMs makes our subsystem compatible with WDM PONs [58].

4.6 Experimental Setup

The experimental setup is illustrated in Fig. 4.2. A Cobrite external cavity laser source with 100 kHz linewidth is split via a 3-dB coupler. One of the coupler output ports is connected to an SHF IQ modulator to generate the SSB downlink signal; the IQ modulator is biased at the null point to suppress the carrier in this branch. The other coupler output is used as the distributed carrier, with a variable optical attenuator (VOA) to adjust signal-to-carrier ratio.

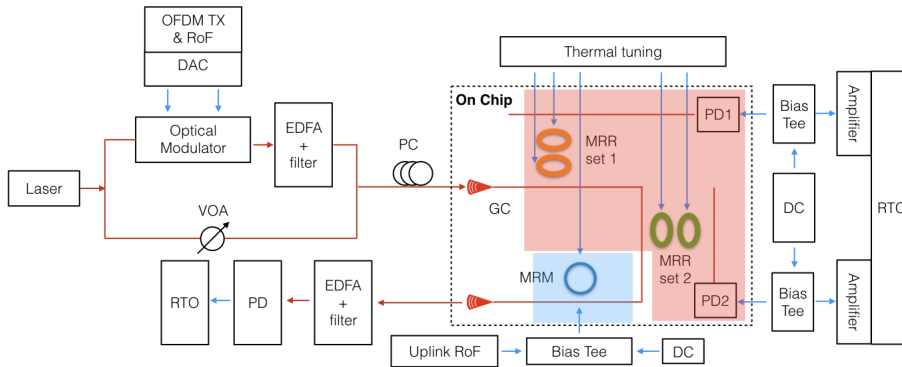


Figure 4.2: Experimental setup to test subsystem.

The RoF and OFDM downlink signals (both QPSK) are generated offline with Matlab and sent to a digital to analog converter (DAC). The FFT size is 1024, covering 64 GHz (DAC sampling rate is 64 GS/s). The wideband OFDM signal includes 127 subcarriers, occupying just under 8 GHz, with an 8 GHz guard band. The complex coordinates of single sideband (SSB) OFDM are generated using two 8-bit DAC channels. The net bit rate for broadband SSB-OFDM transmission is 16 Gb/s and we use direct detection. The narrowband RoF signal is made from five 125 MHz RF signals spaced at 250 MHz and occupying a total bandwidth of 2 GHz within the guard band.

Clipping (5 dB peak-to-average threshold) and pre-compensation are used to compensate the limited dynamic range and bandwidth of the DAC, particularly in the presence of OFDM high peak-to-average power ratio. An Inphi amplifier amplifies the DAC output. The SHF IQ modulator generates the optical SSB signal that is amplified by an erbium doped fiber amplifier (EDFA) and then filtered by a 0.7 nm bandpass filter to suppress amplified spontaneous emission from the EDFA.

The downlink signal is coupled into the chip via a 250 μm spaced fiber array. A polarization controller is used before coupling as the grating couplers (GCs) are polarization sensitive. Our choice of the polarization-sensitive grating coupler for experimental convenience required us to include a polarization controller before coupling. A second generation of the subsystem would use an edge coupler with no polarization sensitivity, and greatly reduce coupler loss.

The integrated subsystem (on-chip portion) is demarcated by the dotted rectangle. The red shading shows the sections for downlink detection, while blue shading is for uplink generation. The downlink detection section includes two sets of cascaded MRRs and two on-chip PDs. Each MRR set drops the desired signal (RoF or OFDM) to the PD. The four MRRs are thermally controlled to achieve the desired frequency response shape. The PDs are reverse-biased with 3V via bias-tees. The electrical signals are amplified and captured by a real-time-oscilloscope (RTO) with a 40 GS/s sampling rate and a 32 GHz RF front end via the RF

probe.

The uplink section is a p-i-n based MRM to remodulate the residual carrier. A separate DAC output is used for the uplink RoF signal; it is amplified and probed onto the MRM. The MRM wavelength is thermally tuned to match the residual carrier. The remodulated uplink signal is coupled out of the chip via the fiber array and then amplified by an EDFA. An off-chip PD with a transimpedance amplifier is used to detect the RoF uplink signal that is captured on a separate RTO channel and processed offline with standard digital signal processing (DSP).

4.7 Hybrid Broadband and RoF detection

4.7.1 Characterization of cascaded MRs

We use two MRR cascaded pairs with similar designs to drop the downlink RoF and OFDM signals. The layout of a cascaded MRR pair with a symmetric structure is shown in Fig. 4.3(a). The ring radii are $10\ \mu\text{m}$; a $13\ \mu\text{m}$ linear waveguide introduced into the rings creates oval structures, resulting in free space range (FSR) around $6\ \text{nm}$. The gap between the rings and the waveguide is $210\ \text{nm}$, while there is a $315\ \text{nm}$ gap between the two rings. These gaps are the only difference between the MRR sets. The first MRR set requires very sharp notch shape response to drop the narrowband RoF signal and a part of the carrier power. To drop the wide band OFDM signals, the second MRR has a gap between the rings and the waveguide of $200\ \text{nm}$, and a gap between the two rings of $305\ \text{nm}$. The smaller gap gives higher coupling efficiency, yielding a more shallow response to cover a wider frequency range.

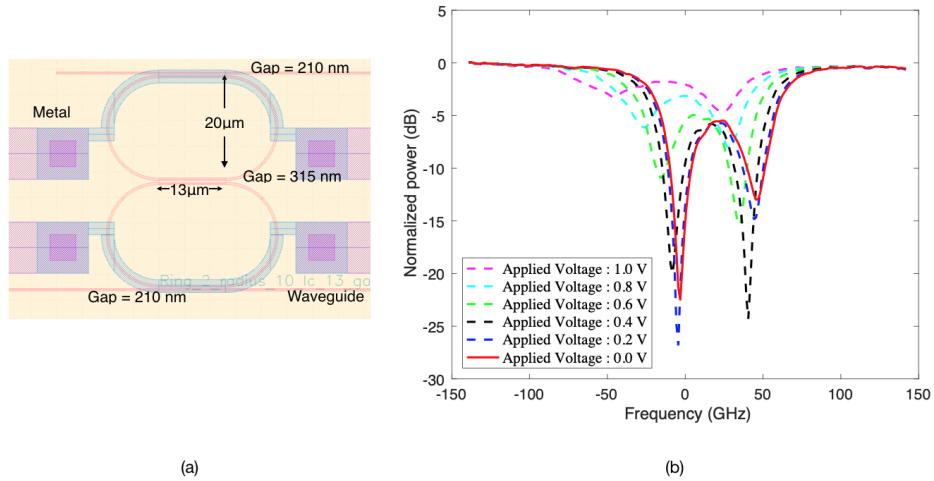


Figure 4.3: (a) Mask layout of MRR set1; (b) MRR responses with thermal tuning

Fig. 4.3(b) shows the cascaded MRR through port response (red solid curve) and the responses (dotted curves) when sweeping the voltage on one of the two heaters. By applying different voltages to each heater, we could control the red shift of the response and move the response peak to the desired frequency. More importantly, by heating the two rings in the cascade

independently, we could change the overall response from sharp notches (extinction ratio more than 25 dB) to a shallow shape. This allows us to control the carrier power dropped, and to select the component of the downlink signal to route to the photodetector. The resonance peaks from the two constituent MRRs in the cascade are spaced by more than 50 GHz, large enough to ensure the signal is filtered by only one notch.

4.7.2 Hybrid Broadband and RoF detection

Figure 4.4 shows the optical spectrum at three different points in the red shaded portion of Fig. 4.2. The spectrum of the signal at the chip input is given in black. We see the carrier at 1557.03 nm, the five separate RoF signals directly to the left, and finally the 8 GHz wide SSB-OFDM signal farther to the left at the end of the guard band. The frequency responses of two MRR sets, $H(f)_{MRRset1}$ and $H(f)_{MRRset2}$, are sketched in dotted orange and green lines, respectively. An inset zooms in on the carrier to show how much of carrier power is dropped at various points along the chip.

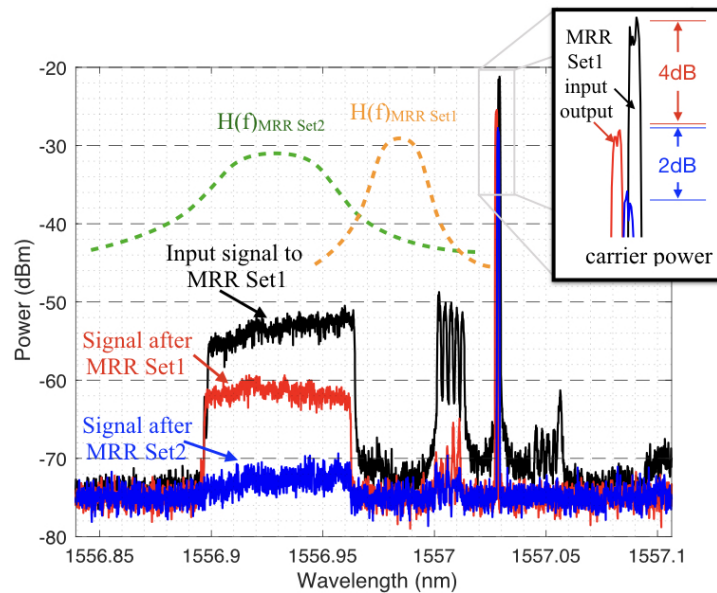


Figure 4.4: Optical spectrum at three measurement points: black curve is input to chip, red curve is output of MRR set 1, blue curve is output of MRR set 2; frequency responses of each set of cascaded MRRs are sketched in dotted lines; an inset zooms on the carrier to show carrier power dropped by MRRs.

4.7.3 RoF detection

The two rings in the cascade are tuned to achieve critical coupling, thus creating a very narrow and deep notch in the through port. The notch is centered on the RoF signal to minimize its residual going to the next section. The dotted orange curve in Fig. 4.4 above the five RoF

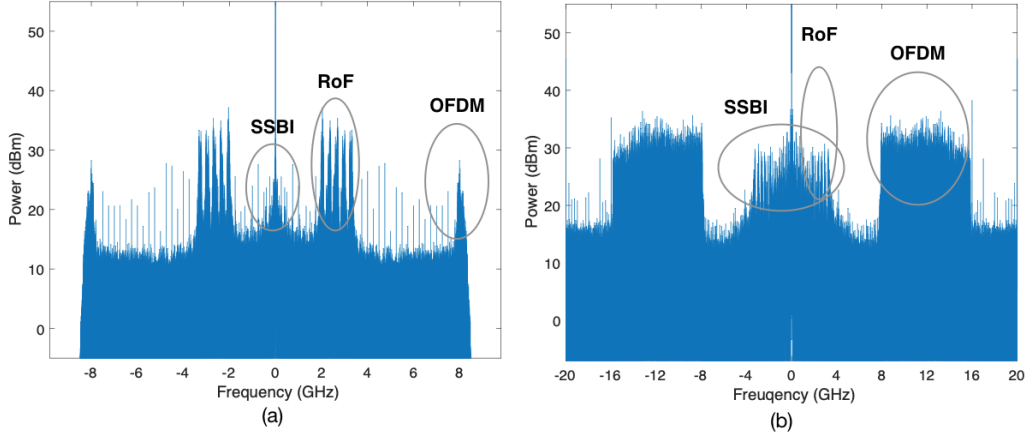


Figure 4.5: Electrical spectrum of detection of (a) RoF signal, (b) OFDM signal.

signals labeled $H(f)_{MRRset1}$ is the approximate drop port frequency response of the first set of MRRs. We drop a small portion of carrier and the entire RoF signal to the PD. The tuning was used to maximize RoF detection with minimal attenuation of the OFDM signal. The amount of carrier dropped could also be adjusted in this manner. As silicon photonics cannot yet offer mature on-chip amplification, preservation of carrier power is important to enable this integrated solution for uplink transmission. The resonance peak of MRR set1 is tuned slightly away from the carrier to let more carrier power pass the MRR set1 at the sacrifice of the downlink signal detection performance.

The red curve in Fig. 4.4 shows the spectrum after the RoF signal is dropped, i.e., the signal entering the second set of cascaded MRMs. We observe around 20 dB suppression of the RoF signal. To combat the anticipated filtering effect of MRR set1 on the OFDM signal, additional power was assigned to the first subcarriers of OFDM signals (see upward tilt in black curve in Fig. 4.4), i.e., a form of pre-emphasis. With this precaution, there is little degradation of the OFDM signal; the red OFDM spectrum is flat. We see in the inset that the carrier power was reduced by only 4 dB, sufficient for RoF reception.

The photodetected electrical spectrum of the RoF signal is given in Fig. 4.5(a). We set the RTO built-in low pass filter to 8 GHz and capture the detected signal at 20 GS/s. An attenuated version of the OFDM signal is dropped (the lowest frequency subcarriers are visible in the electrical spectrum). The residual OFDM results in interference at base band (lower than 1 GHz). The five RoF signals at 2 GHz are unaffected by this interference that can be easily filtered out. To reflect the nature of a 5G receiver, the captured RF signal are down-sampled to 8 GS/s and digitally filtered to separate the five RoF channels. Only a small FFT size (128) is needed. For all five channels the bit error rate (BER) is well under the forward error correction (FEC) threshold. The Q-factor calculated from measured BER of the five RoF channels is 9.57 dB, 10.51 dB, 11.71 dB, 10.88 dB, 11.85 dB from low to high frequency.

4.7.4 Broadband detection

The strategy for OFDM detection is simple. As illustrated by the green dotted line in Fig. 4.4, we tune the second set of MRRs to a shallow shape to allow a wide, flat pass-band for OFDM. The resonance peak is slightly tuned away the carrier instead of falling on the center of OFDM signal band, allowing lower dropped carrier power. The blue curve in Fig. 4.4 shows the optical spectrum at the output of the OFDM drop stage, i.e., after MRR set 2. The downlink OFDM signal is well suppressed, and the carrier power has only decreased by 2 dB. The OFDM signal is captured by the RTO at 40 GS/s and 32 GHz electrical bandwidth. The normal FFT size (1024) is used. The photodetected electrical spectrum of the OFDM signal is given in Fig. 4.5(b). The SSBI falls into the guard band, as well as residual RoF. The BER is 3.2×10^{-3} , below the 7% FEC threshold.

4.8 Carrier Reuse

4.8.1 Characterization of MRM

Figure 4.6(a) shows the partial mask layout including the MRM; a zoom shows the p-i-n structured MRM. The MRM has diameter of $20 \mu\text{m}$, and a gap between the ring and waveguide of 300 nm. In contrast to the other silicon based modulators, our choice of carrier injection based p-i-n modulator provides higher modulation depth and larger changes of refractive index in micron-size footprint [59]. Though the bandwidth of the p-i-n modulator is limited due to the slower diffusion of minority carriers, the low swing voltage [60; 61] is still attractive for OLT applications.

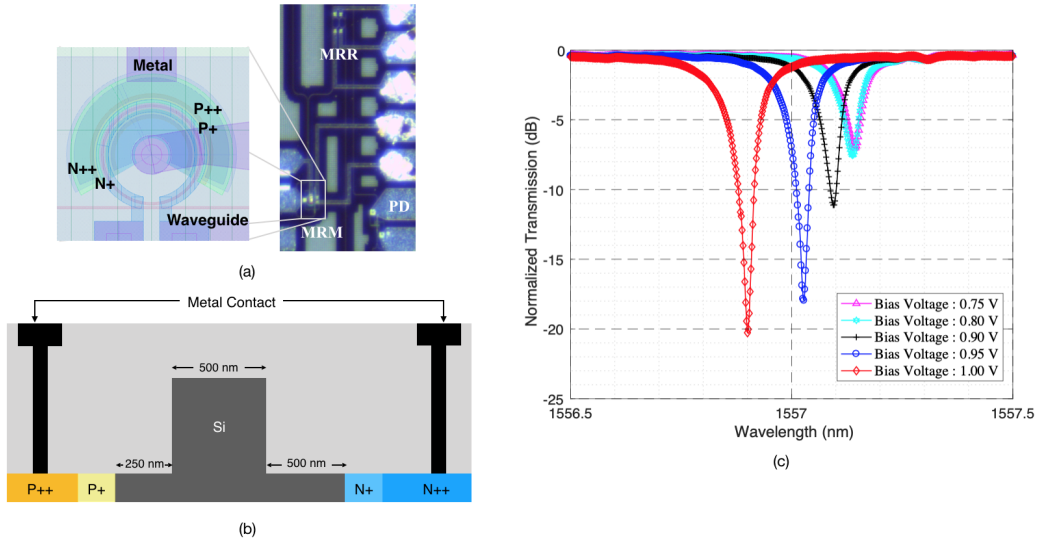


Figure 4.6: MRM (a) partial mask layout, (b) cross section showing relevant dimensions, and (c) measured power transmission spectra at different bias voltages.

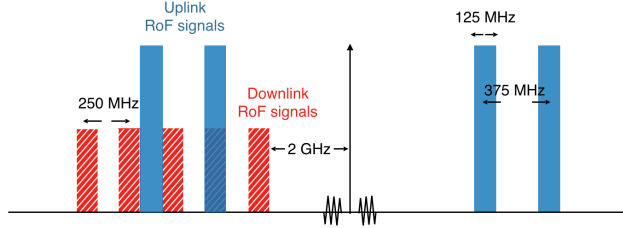


Figure 4.7: Uplink RoF signals with downlink RoF signals

The cross section of the MRM is illustrated in Fig. 4.6(b). Highly doped P (P^{++} , P^+) and N regions (N^{++} , N^+) are separated by the intrinsic region formed by the waveguide. The waveguide width is 500 nm while the gaps between the P^+/N^+ region and waveguide are 250 nm and 500 nm respectively.

The measured optical transmission spectra of the MRM for various bias voltages are presented in Fig. 4.6(c). The pink curve with triangle markers shows the spectrum with forward bias (0.75 V) on the p-i-n junction. The bias voltage is still lower than the built-in potential of the junction. The spectrum shows a resonance depth of around 9 dB at 1557.15 nm. As the forward bias voltage increases, the electron-hole pair density in the cavity increases. Significant blue shifts are observed with larger bias voltage. The MRM is designed in the over-coupling region. Though the increasing electrons and holes result in stronger optical absorption, the depths of the notches are increased due to the lower effective index. The MRM is forward biased at 0.85 V in our experiments.

4.8.2 Remodulation results

We examine the remodulation of the carrier by an uplink RoF signal with two RF sub-components one at 2.25 GHz from the carrier and the other at 2.625 GHz. The limited bandwidth of the p-i-n structured MRM leads to the 2.625 GHz signal having poorer performance; we therefore apply pre-emphasis. We inject a pure carrier into the chip to find the appropriate pre-emphasis and confirm similar performance without downlink signals present.

To examine the impact of residual downlink signals on uplink RoF, we have carefully chosen the uplink RoF signal location. Figure 4.7 illustrates the uplink signal allocations as well as the downlink RoF signals. The hashed, red rectangles represent the downlink RoF signals described previously: five 125 MHz RoF signals over 2 GHz with 250 MHz spacing. The solid blue blocks are the uplink signals, two 125 MHz RoF signals located at 2.25 GHz and 2.625 GHz from the carrier. This choice ensures that one uplink RoF channel is free from residual downlink RoF signals, while the other uplink RoF channel is totally overlapping a downlink RoF signal.

Consider first the pre-emphasized RoF uplink on a distributed carrier when no downlink signal

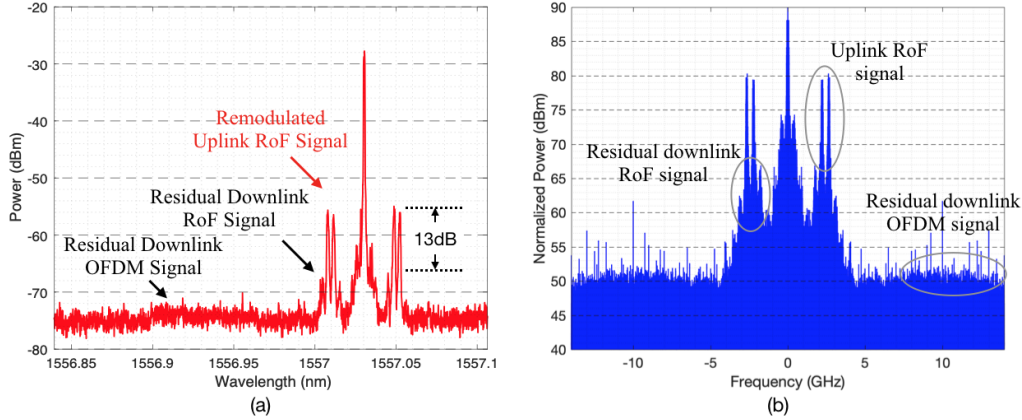


Figure 4.8: Remodulated uplink signal (a) optical spectrum and (b) electrical spectrum

is present. We accomplish this on our chip with DC voltages applied on the MRRs to tune the responses out-of-band. Hence we will see only the losses, but no filtering effects from the two MRR sets.

Next we add the downlink RoF and OFDM signals to the distributed carrier at the input of the MRM. To suppress the downlink signals, we set the DC voltages on the MRR heaters back to the values we used for RoF detection and OFDM detection. The MRR pairs drop the downlink RoF and OFDM signals and leave a clean carrier for remodulation.

Figure 4.8 shows the optical spectrum of the remodulated uplink signal as well as the residual downlink signal under this scenario. The resonance peak of the MRM is tuned to the carrier location. After proper pre-emphasis of the DAC output for the uplink RF signals, two uplink RoF channels with similar power are generated by remodulating the carrier. The downlink signals are well-suppressed by the subsystem, with residual RoF and OFDM signals with limited power observed in Fig. 4.8(a). The generated uplink RoF signal is 13 dB over the downlink signals, indicating their robustness against the crosstalk from residual downlink signals.

The modulated uplink signal is coupled out of chip via the fiber array. The light is amplified by an EDFA and passes through a 0.7 nm optical filter before photodetection. The directly detected electrical signal is captured by the RTO. We count errors and infer the Q-factor from the measured BER.

The direct detection uplink signal faces possible impairment from residual downlink signals. The residual downlink RoF signal could cause direct, in-band crosstalk to the uplink. The residual OFDM signal, while out-of-band, could lead to SSBI covering the whole guard band including the RoF uplink. Figure 4.8(b) presents the electrical spectrum at the uplink receiver. The downlink OFDM signal and the RoF signals both receive significant suppression. Two

uplink RoF signals can be distinguished from the residual downlink RoF signals.

As there is good suppression of the downlink signal, there is no appreciable SSBI. The good suppression of the downlink RoF signals leads to little impairment in the uplink signal. The calculated Q-factors for the two uplink RoF signals are 13.77 dB and 14.12 dB, which confirms hybrid detection is compatible with providing the carrier reuse for uplink signal modulation.

4.8.3 Discussion

This work is a proof of concept of SiP-based direct detection transceiver. The power budget is the main limiting factor in our experiment. The round trip coupling loss is large (13 dB), however this could be reduced to less than 3 dB with mature commercial packaging.

To simplify the experiment, our OFDM signal had a guard band as wide as the signal bandwidth (8 GHz). The guard band could be reduced to improve spectral efficiency, leaving only sufficient bandwidth for the RoF signals. Considering an RoF signal at 2 GHz, a 4 GHz guard band would be sufficient spacing between the downlink signal and RoF signal. The spectral efficiency would be increased from 0.5 to 0.75. With more precise filtering, the guard band could be further decreased. For instance, higher order ring structures have been shown to work well as re-configurable filters. As discussed previously, the detected RoF signal degradation is induced by residual broadband signal intended for the drop port.

Once the specific system parameters are set, we could determine an appropriate trade-off of the uplink carrier power and the residual downlink signal. In our proof of concept, we did not optimize the power assignment. The performance requirement for downlink and uplink transmission would determine the final strategy for the power budget. For example, in a transceiver the transmitter typically requires 70% of laser power. In our system, this would mean reserving 70% of the received carrier for remodulation, with the residual going to signal reception. We used 6 dB (75%) of the carrier for detection. The detection of RoF signal contributed to 4 dB carrier attenuation, i.e., even higher than OFDM detection. We could reduce RoF carrier requirements by about 2 dB by implementing a higher order MRR. Depending on uplink signal performance requirements, we could further decrease the carrier power for detection. Note that in a PON, the uplink could benefit from the greater sensitivity of coherent detection at the central office where laser sources are available. Hence, for a PON with a colorless ONU, the allocation of greater power resources to reception could be manageable.

We note the downlink signal in Fig. 4.4 shows greater suppression of the dropped RoF signal than we see after remodulation in Fig. 4.8; the difference is about 2 dB. The very limited bandwidth of the p-i-n modulator also induces some nonlinear distortion near the carrier, leading to some undesired out-of-band components. The slightly stronger residual RoF signals could be the result of thermal crosstalk. We apply a 4V voltage to the MRM heater, which heats the MRR pairs and causes a shift in the passband.

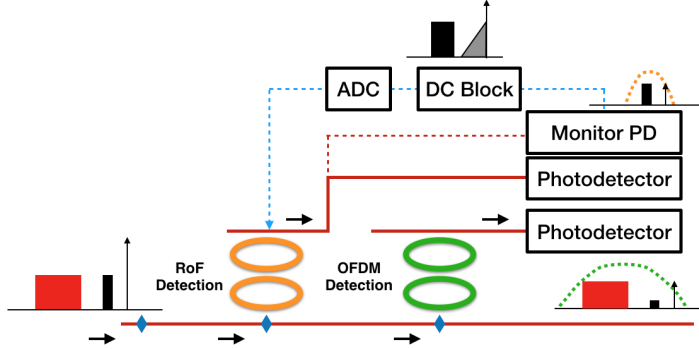


Figure 4.9: Automatic Ring Control

To address both thermal crosstalk and fabrication variations in the ring resonator, a feedback loop could be added to future subsystems. Due to the sensitivity of SiP components, automatic feedback control loop is generally required for commercial SiP products. For example, precise heating on ring resonators is demonstrated in [62]. Though ring-based structures are more vulnerable to temperature changes, they are still attractive for their ultra compact size and routing functions.

An automatic feedback control loop could be easily incorporated into our SiP structure, as illustrated in Fig. 4.9. A directional coupler guides a small portion of the RoF drop port to a monitor PD. The feedback loop must match the passband of the ring resonator to the RoF signal. The dropped signal has RoF as well as SSBI from the RoF signal, as sketched above the DC block element. The power of the detected RoF signal (black shaded rectangle) is determined by the dropped RoF and carrier power. The SSBI (grey shaded triangle) is determined on by the dropped RoF signal power. By monitoring the SSBI signal power, the passband of the rings could be tuned to the RoF signals. The SSBI signal could be monitored easily by using a low rate ADC with a low pass response rejecting the RoF signal.

Our all-silicon solution cannot take advantage of on-chip amplification. Therefore our proposed subsystem husbands the carrier power; it has the downlink signal dropped via MRR pairs for detection and avoids splitters. By designing the MRR with higher quality factor, better separation of the carrier and downlink signal could be realized to improve the downlink detection performance and the uplink remodulation simultaneously.

4.9 Conclusion

We have proposed a novel silicon photonics subsystem supporting detection of RoF signals as well as the principle broadband signal. The proposed subsystem enables heterogeneous services and conserves carrier power to enable remodulation of uplink RF signals within a single feeder PON architecture. The subsystem is fabricated and experimentally validated. Five 125 MHz

RoF signals and one 7.75 GHz OFDM downlink signal are detected simultaneously on-chip. Two 125 MHz RoF signals are generated by reusing the carrier via an on-chip MRM. The performance degradation on the uplink RoF signal induced by residual RoF downlink signal is only on the order of one half dB.

Conclusion and Outlook

II.1 Conclusion

At present, PON is undoubtedly the workhorse of optical distributed networks. In this thesis, we discussed the evolution of next generation PONs from two perspectives, higher performance and new services. The evolution of next generation PONs should be low cost, which is the cornerstone of PON.

We chose SiP technology as the enabling technique to realize the smooth and low cost upgrade of PONs. The SiP technique is compatible with mature CMOS manufacturing, allowing high volume and reliable production with a cheap material, silicon. The dimensions of SiP PICs is typically only several millimeters per side, which leads to very small size chips. However, the SiP technique has its own drawbacks including the sensitivity to temperature and polarization state. In this thesis, we take account of those limits when we design the SiP subsystems for practical uses.

In this thesis, we demonstrated several silicon photonics solutions for the evolution of next generation PON. We started from enhancing performance of current broadband services on PON. We examined directly detected OFDM for broadband services. To increase the transmission distance, we focused on the CD problem. To avoid the CD-induced power fading, we generated the SSB OFDM with an on-chip subsystem. Using IQ configured MRMs, we generated the SSB OFDM signal with over 18 dB sideband suppression ratio. We choose the MRM instead of MZM to decrease the footprint of PICs as well as the power consumption.

In addition to the CD problem, SSBI also limits the transmission distance of DD system. The sacrifice of spectral or power efficiency is not acceptable in low cost PON scenarios, hence we examined a hardware solution for SSBI. We eliminated discrete and bulky components by moving to a SiP platform. With our proposed subsystem, we experimentally demonstrated good SSBI cancellation performance under ultra low CSR of 0 dB. By lowering the carrier power requirement, our solution supports more flexible power assignments in PON and longer transmission distance with limited carrier power.

The non-ideal filtering effect as well as the intrinsic drawbacks of SiP are considered as the

main limits for practical uses. In the first work on SSBI, which is demonstrated in chapter 2, we introduced a scaling factor to the balanced detection to trade-off the non-ideal filtering. In the experimental demonstration we allowed the resonant frequency to drift by as much as 12 GHz from the targeted value with that design, and still provided good performance.

Following the validation of first work on SSBI, we further studied the SSBI cancellation scheme to provide a generic guide to design. To deal with the polarization sensitivity, we discussed adding polarization diversity to the subsystem. By introducing a new performance metric, minimum guaranteed Q-factor, we re-evaluated the SSBI cancellation performance with signal format parameters: the guard band value, modulation format, MRR design parameters and the tuning of frequency. With the development of next generation PON, diverse PON architects could coexist in the future with different requirements of power, data rate and other considerations. Our systematic simulation on the SSBI cancellation subsystem can guide the optimization of data rate or robustness for different practical uses.

Our second research focus on PON is to support RAN. Existing PON deployment is an excellent resource for supporting optical networks for 5G. The point-to-multipoint structure of PON alleviates the burden of linking a large number of small cells for 5G. Our focus on RAN was the overlay of 5G signals on a PON infrastructure for RAN. In this thesis we experimentally demonstrated the simultaneous detection of coexisting RoF signal and broadband OFDM signals, as well as the remodulation of the carrier for uplink. Using tunable MRRs, this subsystem enables the flexible detection of future RAN traffic as well as the traditional PON traffic over the same assigned wavelength slot. The subsystem drops a clean carrier for remodulation to generate the uplink signal. Our proposed subsystem exhibits the potential to support full duplex transmission without active components like laser or reflective semiconductor optical amplifier. All the functions are integrated on a single chip, yielding a low cost transceiver for next generation PON supporting new data stream.

II.2 Improved Designs for Future Work

We have submitted new designs for the subsystems described in the thesis. The polarization diverse solution in particular has seen two cycles of design/fabrication. The layout was improved for better experimental exploitation. New designs also included support of several new features. The full layout is shown in Fig. II.1.

In Fig. II.1, the designs marked as 1, 2 and 3 are three test structures. The first one is the cascaded MRRs. The second is the PSR, while the last one is the IQ modulator. The test structures facilitate characterization of the fundamental components.

II.2.1 Addressing polarization diversity

In chapter 4, we mentioned that the future PON should be a single feeder structure. That chip design, however, had an input and an output port. In our new design we attack the more challenging single port for both input and output (compatible with a single feeder network).

The design marked as No.4 in Fig. II.2 is the transceiver with polarization diversity. Instead of guiding the remodulated uplink signal, we use the PSR as a routing component to realize a single feeder structure. The function of this design includes:

- PSR for the polarization splitting and rotation
- Identical cascaded MRRs drops for the downlink signal to the same PD

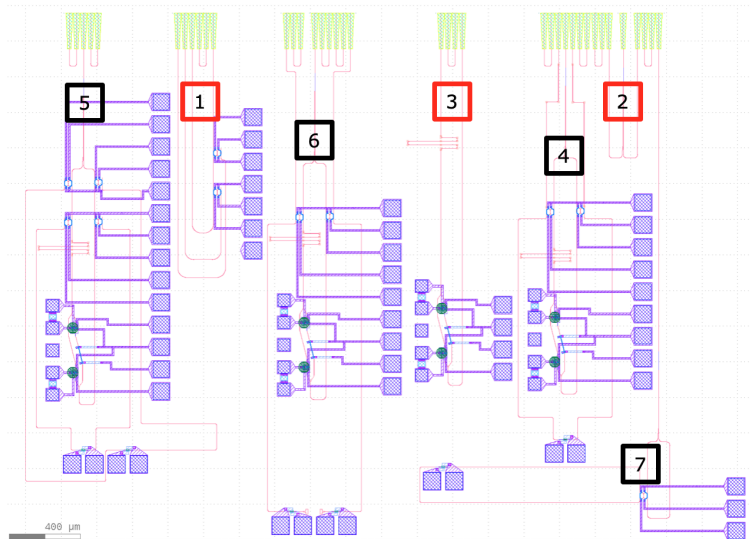


Figure II.1: Layout of full design

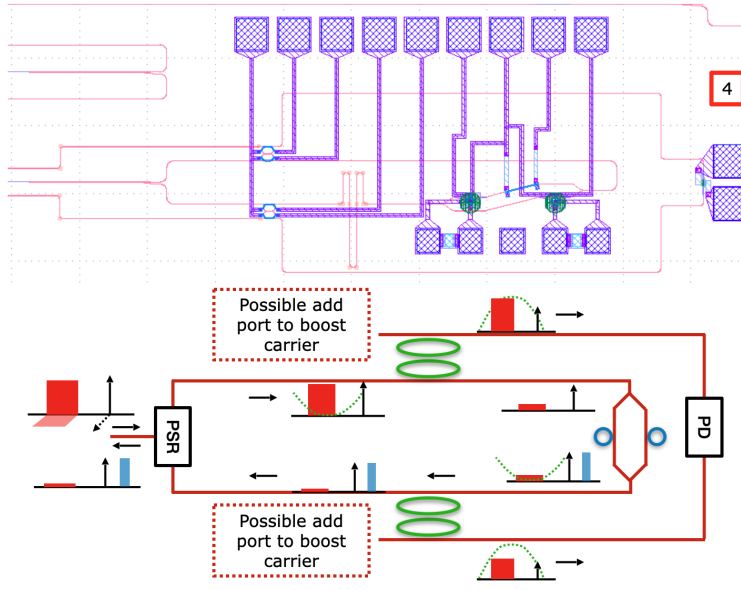


Figure II.2: Layout of transceiver with polarization diversity

- IQ MRM with matched waveguide length to enable uplink generation with smeared time signals

As we discussed in chapter 4, we add the compatibility of 5G RoF signal for the transceiver. This is illustrated in Fig. II.3. We add another set of cascaded MRRs and PD to enable RoF detection.

We note that our approach to detection could also be used to enable the KK detector in a polarization diverse SiP solution. The KK detector is also included in the layout, which is illustrated in Fig. II.4. The function of this design includes:

- Add port enables the carrier boosting
- After PSR, signals on different polarization state are sent to different PDs

Finally, we were inspired to use the routing function of MRR. In the polarization diversity in the designs just described we use a PSR and identical components on two duplicated paths. We add a new design to achieve the polarization diversity with reduced devices using MRR routing, as illustrated in Fig. II.5. After the PSR split, a single MRR is passed. Thus when the waveguide is matched, the polarization diversity could be realized with only one copy of the device.

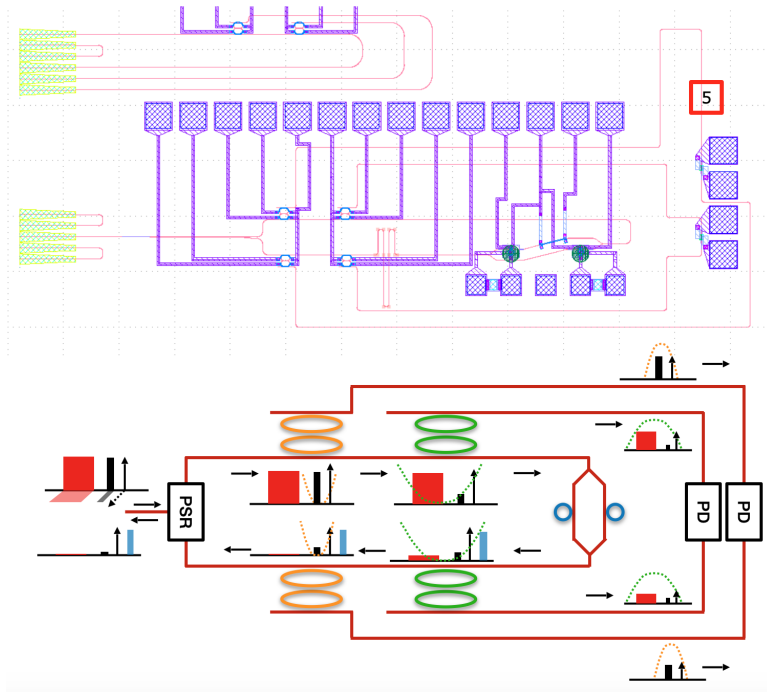


Figure II.3: Layout of 5G transceiver with polarization diversity

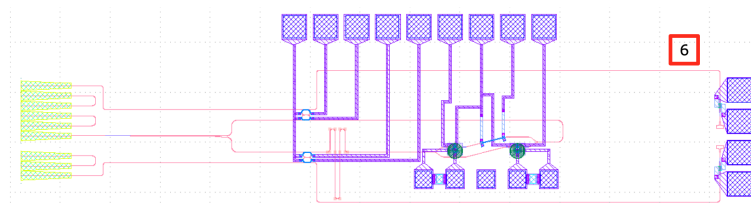


Figure II.4: Layout of polarization division multiplexing with KK scheme

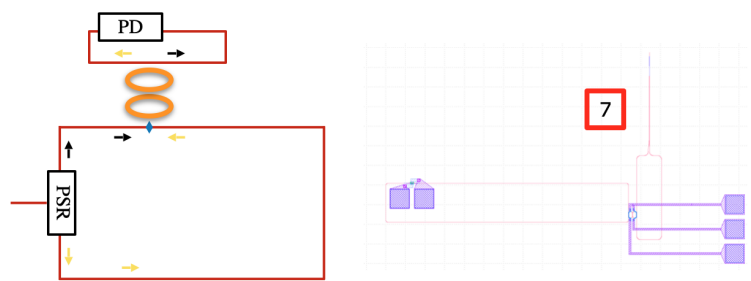


Figure II.5: Layout of polarization solution with reduced devices

Publication list

Published papers

1. Lyu, Mingyang , S. Amiralizadeh , and L. A. Rusch. "Constellation-induced SNR gain in short-reach optical OFDM." *2016 IEEE Photonics Conference (IPC)* IEEE, 2016.
2. Lyu, Mingyang , and L. A. Rusch. "Silicon photonics enabled SSBI cancellation." *2017 IEEE Photonics Conference (IPC)* IEEE, 2017.
3. Lyu, Mingyang , et al. "Experimental examination of ssbi suppression using SiP microring resonators." *2017 International Topical Meeting on Microwave Photonics (MWP)* IEEE, 2017.
4. Lyu, Mingyang , W. Shi , and L. A. Rusch. "SiP Alternative to Enhanced KK for OFDM." *2018 European Conference on Optical Communication (ECOC)*, 2018.
5. Lyu, Mingyang , W. Shi , and L. A. Rusch. "SiP-Based SSBI Cancellation for OFDM." *Photonics Journal*, IEEE 11.5(2019):1-13.
6. Lyu, Mingyang , W. Shi , and L. A. Rusch. "Silicon Photonics to Add 5G RoF Services to PONs Employing Carrier Reuse." *Optical Fiber Communication Conference 2020*.
7. Lyu, Mingyang , W. Shi , and L. A. Rusch. "Silicon Photonic Subsystem for Broadband and RoF Detection While Enabling Carrier Reuse." *Optics Express*, 28.10(2020).
8. Xu, Yelong, Lyu, Mingyang , et al. "Generation of Optical Single Sideband OFDM Using a Silicon Microring IQ modulator." *Cleo: Applications & Technology 2018*, 2018.
9. Lyu, Mingyang , et al. "Single-Sideband OFDM Transmission via a Silicon Microring IQ Modulator." *IEEE Photonics Technology Letters*, (2018).
10. Guan, Xun ,Lyu, Mingyang , et al. "Silicon Photonics for 5G Passive Optical Networks." *2019 IEEE 10th Annual Information Technology, Electronics and Mobile Communication Conference (IEMCON)*, 2019.

Papers under review

11. Mingyang Lyu, Wei Shi and Leslie A. Rusch. "Optimizing SiP Microring Resonators to Suppress Interference in OFDM Detection." *OE*.

Bibliography

- [1] IDC, “Idc’s global datasphere forecast shows continued steady growth in the creation and consumption of data = <https://www.idc.com/getdoc.jsp?containerid=prus46286020>, year = 2020,.”
- [2] Omidia, “Pon-based broadband is winning with future divergence concerns = <https://omdia.tech.informa.com/om017022/pon-based-broadband-is-winning-with-future-divergence-concerns>, year = 2021,.”
- [3] J.-i. Kani, F. Bourgart, A. Cui, A. Rafel, M. Campbell, R. Davey, and S. Rodrigues, “Next-generation pon-part i: Technology roadmap and general requirements,” *IEEE Communications Magazine*, vol. 47, no. 11, pp. 43–49, 2009.
- [4] I. Chih-Lin, H. Li, J. Korhonen, J. Huang, and L. Han, “Ran revolution with ngfi (xhaul) for 5g,” *Journal of Lightwave Technology*, vol. 36, no. 2, pp. 541–550, 2017.
- [5] LightCounting, “Adoption of silicon photonics is reaching an inflection point,” <https://www.lightcounting.com/light-trends/adoption-silicon-photonics-reaching-inflection-point/>, 2020.
- [6] B. J. Schmidt, Z. Zan, L. B. Du, and A. J. Lowery, “100 gbit/s transmission using single-band direct-detection optical ofdm,” in *National Fiber Optic Engineers Conference*. Optical Society of America, 2009, p. PDPC3.
- [7] W.-R. Peng, X. Wu, V. R. Arbab, K.-M. Feng, B. Shamee, L. C. Christen, J.-Y. Yang, A. E. Willner, and S. Chi, “Theoretical and experimental investigations of direct-detected rf-tone-assisted optical ofdm systems,” *Journal of Lightwave Technology*, vol. 27, no. 10, pp. 1332–1339, 2009.
- [8] J.-H. Yan, Y.-W. Chen, B.-C. Tsai, and K.-M. Feng, “A multiband ddo-ofdm system with spectral efficient iterative ssbi reduction dsp,” *IEEE Photonics Technol. Lett.*, vol. 28, no. 2, pp. 119–122, 2016.
- [9] W.-R. Peng, I. Morita, and H. Tanaka, “Enabling high capacity direct-detection optical ofdm transmissions using beat interference cancellation receiver,” in *Optical Communi-*

- cation (ECOC), 2010 36th European Conference and Exhibition on. IEEE, 2010, pp. 1–3.
- [10] S. A. Nezamalhosseini, L. R. Chen, Q. Zhuge, M. Malekiha, F. Marvasti, and D. V. Plant, “Theoretical and experimental investigation of direct detection optical ofdm transmission using beat interference cancellation receiver,” *Optics express*, vol. 21, no. 13, pp. 15 237–15 246, 2013.
- [11] D. Bladsjö, M. Hogan, and S. Ruffini, “Synchronization aspects in lte small cells,” *IEEE Communications Magazine*, vol. 51, no. 9, pp. 70–77, 2013.
- [12] J. Lin, J. B. Mueller, Q. Wang, G. Yuan, N. Antoniou, X.-C. Yuan, and F. Capasso, “Polarization-controlled tunable directional coupling of surface plasmon polaritons,” *Science*, vol. 340, no. 6130, pp. 331–334, 2013.
- [13] G. Meslener, “Chromatic dispersion induced distortion of modulated monochromatic light employing direct detection,” *IEEE Journal of Quantum Electronics*, vol. 20, no. 10, pp. 1208–1216, 1984.
- [14] L.-S. Yan, C. Yu, Y. Wang, T. Luo, L. Paraschis, Y. Shi, and A. Willner, “40-gb/s transmission over 25 km of negative-dispersion fiber using asymmetric narrow-band filtering of a commercial directly modulated dfb laser,” *IEEE photonics technology letters*, vol. 17, no. 6, pp. 1322–1324, 2005.
- [15] G. H. Smith, D. Novak, and Z. Ahmed, “Overcoming chromatic-dispersion effects in fiber-wireless systems incorporating external modulators,” *IEEE transactions on microwave theory and techniques*, vol. 45, no. 8, pp. 1410–1415, 1997.
- [16] W. Shi, Y. Xu, H. Sepehrian, S. LaRochelle, and L. A. Rusch, “Silicon photonic modulators for PAM transmissions,” *Journal of Optics*, vol. 20, no. 8, p. 083002, 2018.
- [17] R. Dubé-Demers, S. LaRochelle, and W. Shi, “Ultrafast pulse-amplitude modulation with a femtojoule silicon photonic modulator,” *Optica*, vol. 3, no. 6, pp. 622–627, 2016.
- [18] P. Dong, C. Xie, L. Chen, N. K. Fontaine, and Y.-k. Chen, “Experimental demonstration of microring quadrature phase-shift keying modulators,” *Optics letters*, vol. 37, no. 7, pp. 1178–1180, 2012.
- [19] C. Y. Wong, S. Zhang, Y. Fang, L. Liu, T. Wang, Q. Zhang, S. Deng, G. N. Liu, and X. Xu, “Silicon iq modulator for next-generation metro network,” *Journal of Lightwave Technology*, vol. 34, no. 2, pp. 730–736, 2016.
- [20] B.-M. Yu, J.-M. Lee, C. Mai, S. Lischke, L. Zimmermann, and W.-Y. Choi, “Single-chip si optical single-sideband modulator,” *Photonics Research*, vol. 6, no. 1, pp. 6–11, 2018.

- [21] Z. Li, M. S. Erkilinç, K. Shi, E. Sillekens, L. Galdino, B. C. Thomsen, P. Bayvel, and R. I. Killey, “Ssbi mitigation and the kramers–kronig scheme in single-sideband direct-detection transmission with receiver-based electronic dispersion compensation,” *Journal of Lightwave Technology*, vol. 35, no. 10, pp. 1887–1893, 2017.
- [22] R. Urata, C. Lam, H. Liu, and C. Johnson, “High performance, low cost, colorless onu for wdm-pon,” in *National Fiber Optic Engineers Conference*. Optical Society of America, 2012, pp. NTh3E–4.
- [23] P. Dong, R. Gatlula, K. Kim, J. H. Sinsky, A. Melikyan, Y.-K. Chen, G. De Valicourt, and J. Lee, “Simultaneous wavelength locking of microring modulator array with a single monitoring signal,” *Optics Express*, vol. 25, no. 14, pp. 16 040–16 046, 2017.
- [24] J. Yu, M.-F. Huang, D. Qian, L. Chen, and G.-K. Chang, “Centralized lightwave wdm-pon employing 16-qam intensity modulated ofdm downstream and ook modulated upstream signals,” *IEEE Photonics Technology Letters*, vol. 20, no. 18, pp. 1545–1547, 2008.
- [25] S. Randel, D. Pileri, S. Chandrasekhar, G. Raybon, and P. Winzer, “100-gb/s discrete-multitone transmission over 80-km ssmf using single-sideband modulation with novel interference-cancellation scheme,” in *Optical Communication (ECOC), 2015 European Conference on*. IEEE, 2015, pp. 1–3.
- [26] Z. Li, M. S. Erkilinç, L. Galdino, K. Shi, B. C. Thomsen, P. Bayvel, and R. I. Killey, “Comparison of digital signal-signal beat interference compensation techniques in direct-detection subcarrier modulation systems,” *Optics express*, vol. 24, no. 25, pp. 29 176–29 189, 2016.
- [27] Z. Li, M. S. Erkilinç, R. Maher, L. Galdino, K. Shi, B. C. Thomsen, P. Bayvel, and R. I. Killey, “Two-stage linearization filter for direct-detection subcarrier modulation,” *IEEE Photonics Technol. Lett.*, vol. 28, no. 24, pp. 2838–2841, 2016.
- [28] Z. Li, M. S. Erkilinç, S. Pachnicke, H. Griesser, R. Bouziane, B. C. Thomsen, P. Bayvel, and R. I. Killey, “Signal-signal beat interference cancellation in spectrally-efficient wdm direct-detection nyquist-pulse-shaped 16-qam subcarrier modulation,” *Optics Express*, vol. 23, no. 18, pp. 23 694–23 709, 2015.
- [29] S. C. C. Mecozzi, Antonelli and Winzer, “The kramers-kronig receiver,” in *Optical Fiber Communication Conference*. Optical Society of America, 2018, pp. Tu2D–1.
- [30] Z. Li, M. Erkilinç, K. Shi, E. Sillekens, L. Galdino, B. Thomsen, P. Bayvel, and R. Killey, “Joint optimisation of resampling rate and carrier-to-signal power ratio in direct-detection kramers-kronig receivers,” in *Proc. ECOC*, 2017.

- [31] L. Blech, Y. Eldar, C. Antonelli, A. Mecozzi, and M. Shtaif, "The enhanced kramers kronig receiver," in *Optical Fiber Communication Conference*. Optical Society of America, 2018, pp. Tu2D–7.
- [32] M. Lyu, X. Guan, and L. A. Rusch, "Experimental examination of ssbi suppression using sip microring resonators," in *Microwave Photonics (MWP), 2017 IEEE International Topical Meeting on*. IEEE, 2017, p. accepted to appear.
- [33] L. Chrostowski and M. Hochberg, *Silicon photonics design: from devices to systems*. Cambridge University Press, 2015.
- [34] R. A. Shafik, M. S. Rahman, and A. R. Islam, "On the extended relationships among evm, ber and snr as performance metrics," in *Electrical and Computer Engineering, 2006. ICECE'06. International Conference on*. IEEE, 2006, pp. 408–411.
- [35] J. K. Poon, J. Scheuer, S. Mookherjea, G. T. Paloczi, Y. Huang, and A. Yariv, "Matrix analysis of microring coupled-resonator optical waveguides," *Optics express*, vol. 12, no. 1, pp. 90–103, 2004.
- [36] M. Lyu, W. Shi, and L. A. Rusch, "Sip alternative to enhanced kramers kronig for ofdm," in *2018 European Conference on Optical Communication (ECOC)*. IEEE, 2018, pp. 1–3.
- [37] X. Chen, S. Chandrasekhar, and P. Winzer, "Self-coherent systems for short reach transmission," in *2018 European Conference on Optical Communication (ECOC)*. IEEE, 2018, pp. 1–3.
- [38] D. Hewitt, "Orthogonal frequency division multiplexing using baseband optical single sideband for simpler adaptive dispersion compensation," in *Optical Fiber Communication Conference*. Optical Society of America, 2007, p. OME7.
- [39] A. J. Lowery, "Improving sensitivity and spectral efficiency in direct-detection optical ofdm systems," in *Optical Fiber communication/National Fiber Optic Engineers Conference, 2008. OFC/NFOEC 2008. Conference on*. IEEE, 2008, pp. 1–3.
- [40] W.-R. Peng, X. Wu, V. R. Arbab, B. Shamee, L. C. Christen, J.-Y. Yang, K.-M. Feng, A. E. Willner, and S. Chi, "Experimental demonstration of a coherently modulated and directly detected optical ofdm system using an rf-tone insertion," in *Optical Fiber communication/National Fiber Optic Engineers Conference, 2008. OFC/NFOEC 2008. Conference on*. IEEE, 2008, pp. 1–3.
- [41] W.-R. Peng, X. Wu, K.-M. Feng, V. R. Arbab, B. Shamee, J.-Y. Yang, L. C. Christen, A. E. Willner, and S. Chi, "Spectrally efficient direct-detected ofdm transmission employing an iterative estimation and cancellation technique," *Optics express*, vol. 17, no. 11, pp. 9099–9111, 2009.

- [42] G. K. Chang, A. Chowdhury, Z. Jia, H. C. Chien, M. F. Huang, J. Yu, and G. Ellinas, “Key technologies of wdm-pon for future converged optical broadband access networks [invited],” *Journal of Optical Communications and Networking*, vol. 1, no. 4, pp. C35–C50, 2009.
- [43] Vincent, Houtsma, Douthje, van, Veen, Ed, and Harstead, “Recent progress on standardization of next-generation 25, 50, and 100g epon,” *Journal of Lightwave Technology*, 2017.
- [44] D. Zhang, D. Liu, X. Wu, and D. Nesses, “Progress of itu-t higher speed passive optical network (50g-pon) standardization,” *Journal of Optical Communications and Networking*, vol. 12, no. 10, pp. D99–D108, 2020.
- [45] J. S. Wey, “The outlook for pon standardization: A tutorial,” *Journal of Lightwave Technology*, vol. 38, no. 1, pp. 31–42, 2020.
- [46] D. V. Veen and V. Houtsma, “Bi-directional 25g/50g tdm-pon with extended power budget using 25g apd and coherent amplification,” in *Optical Fiber Communications Conference and Exhibition*, 2017.
- [47] M. Lyu, W. Shi, and L. A. Rusch, “Silicon photonics to add 5g rof services to pons employing carrier reuse,” in *Optical Fiber Communication Conference*, 2020.
- [48] M. Lyu, W. Shi, and L. Rusch, “Sip-based ssbi cancellation for ofdm,” *IEEE Photonics Journal*, vol. 11, no. 5, pp. 1–13, 2019.
- [49] K. Laraqui, “Small cell optical mobile backhauling: Architectures, challenges, and solutions,” in *39th European Conference and Exhibition on Optical Communication (ECOC 2013)*. IET, 2013, pp. 1–3.
- [50] J.-i. Kani, F. Bourgart, A. Cui, A. Rafel, M. Campbell, R. Davey, and S. Rodrigues, “Next-generation pon-part i: Technology roadmap and general requirements,” *IEEE Communications Magazine*, vol. 47, no. 11, pp. 43–49, 2009.
- [51] C. Chow, C. Yeh, C. Wang, F. Shih, and S. Chi, “Signal remodulation of ofdm-qam for long reach carrier distributed passive optical networks,” *IEEE Photonics Technology Letters*, vol. 21, no. 11, pp. 715–717, 2009.
- [52] J. Yu, O. Akanbi, Y. Luo, L. Zong, T. Wang, Z. Jia, and G.-K. Chang, “Demonstration of a novel wdm passive optical network architecture with source-free optical network units,” *IEEE Photonics Technology Letters*, vol. 19, no. 8, pp. 571–573, 2007.
- [53] Z. Jia, J. Yu, G. Ellinas, and G.-K. Chang, “Key enabling technologies for optical–wireless networks: optical millimeter-wave generation, wavelength reuse, and architecture,” *Journal of Lightwave Technology*, vol. 25, no. 11, pp. 3452–3471, 2007.

- [54] A. Rickman, “The commercialization of silicon photonics,” *Nature Photonics*, vol. 8, no. 8, p. 579, 2014.
- [55] B. Charbonnier, S. Menezo, P. O’Brien, A. Lebreton, J. Fedeli, and B. B. Bakir, “Silicon photonics for next generation fdm/fdma pon,” *Journal of Optical Communications and Networking*, vol. 4, no. 9, pp. A29–A37, 2012.
- [56] N. Cvijetic, “Ofdm for next-generation optical access networks,” *Journal of lightwave technology*, vol. 30, no. 4, pp. 384–398, 2011.
- [57] W. Shi, Y. Xu, H. Sephrian, S. LaRochelle, and L. A. Rusch, “Silicon photonic modulators for pam transmissions,” *Journal of Optics*, vol. 20, no. 8, p. 083002, 2018.
- [58] P. Dong, R. Shafiiha, S. Liao, H. Liang, N.-N. Feng, D. Feng, G. Li, X. Zheng, A. V. Krishnamoorthy, and M. Asghari, “Wavelength-tunable silicon microring modulator,” *Optics express*, vol. 18, no. 11, pp. 10 941–10 946, 2010.
- [59] Q. Xu, S. Manipatruni, B. Schmidt, J. Shakya, and M. Lipson, “12.5 gbit/s carrier-injection-based silicon micro-ring silicon modulators,” *Optics express*, vol. 15, no. 2, pp. 430–436, 2007.
- [60] S. Manipatruni, K. Preston, L. Chen, and M. Lipson, “Ultra-low voltage, ultra-small mode volume silicon microring modulator,” *Optics express*, vol. 18, no. 17, pp. 18 235–18 242, 2010.
- [61] G. T. Reed, G. Mashanovich, F. Y. Gardes, and D. Thomson, “Silicon optical modulators,” *Nature photonics*, vol. 4, no. 8, p. 518, 2010.
- [62] W. S. Fegadolli, G. Vargas, X. Wang, F. Valini, L. A. Barea, J. E. Oliveira, N. Frateschi, A. Scherer, V. R. Almeida, and R. R. Panepucci, “Reconfigurable silicon thermo-optical ring resonator switch based on vernier effect control,” *Optics express*, vol. 20, no. 13, pp. 14 722–14 733, 2012.